Università Degli Studi Di Napoli *Federico II*

PhD Program in Quantum Technologies

XXXVI Cycle

Coordinator: Prof. Francesco Tafuri

Advancements in quantum information: dissipative stabilisation and microwave quantum illumination

Scientific Disciplinary Sector FIS/02

PhD candidate	Tutor
Jacopo Angeletti	Prof. David Vitali

A. Y. 2022-2023

I just need
a way out of my head.

Abstract

Positioned at the forefront of scientific progress, the quantum realm promises transformative advancements, reshaping our responses to intricate challenges. In the dynamic landscape of quantum technologies, this doctoral thesis endeavors to unravel two distinct facets. The first part delves into the complexities of steering a quantum array into a pure steady state, where distant, non-directly interacting qubits become entangled. By artfully manipulating dissipative dynamics on a central element, we not only showcase the attainability of an entangled steady state, but also underscore its resilience to additional decoherence. With broad applications across atomic systems and solid-state nano-devices, this approach allows for the realization of diverse geometries. Shifting focus to the second part, our attention turns to the quantum illumination, addressing imperfections inherent in experimental setups. Here, correlation-to-displacement conversion-based receivers take the spotlight, revealing their efficacy in amplifying return signals to counter losses in heterodyne detection. Notably, a simple Kennedy receiver outperforms classical counterparts in practical settings, presenting a quantum advantage over known quantum receivers. The synthesis of theoretical exploration and practical enhancements contributes meaningfully to the evolving narrative of quantum technologies, marking a distinctive stride towards realizing their potential.

Contents

Introduction

Quantum computation, communication, and simulation have emerged as trailblazers in scientific and technological advancement, ushering in unprecedented possibilities and transforming our approach to intricate challenges. In the dynamic expanse of quantum technologies, a realm where the extraordinary becomes palpable, this doctoral thesis endeavors to illuminate two distinct facets. Anchored by two published articles, each offering insights into different dimensions of the quantum world, our exploration unfolds.

The initial article navigates the process of steering a quantum array into a pure steady state, where many pairs of distant, non-directly interacting qubits become entangled. Through astute manipulation of dissipative dynamics on a singular central element, we not only demonstrate the attainability of an entangled steady state but also unveil its resilience to additional decoherence, affecting neighboring qubits. The practical implications span diverse physical scenarios, encompassing atomic systems and solid-state nano-devices, fostering versatility in realizing various geometries.

Shifting our focus to the second article, we delve into the quantum illumination, aiming to address inherent imperfections in experimental setups. Here, the emphasis is on correlation-to-displacement conversion-based receivers, showcasing their efficacy in amplifying return signals to counter losses in heterodyne detection. Notably, even a simple Kennedy receiver proves superior in practical settings to both classical counterparts, providing a quantum advantage, and known quantum receivers.

Embarking on this analytical journey, the subsequent chapters will dig into the intricacies, methodologies, and profound implications of these investigations. The synthesis of theoretical exploration and practical enhancements contributes meaningfully to the ever-evolving narrative of quantum technologies, offering insightful strides toward unlocking their potential.

Chapter 1

Dissipative stabilization of entangled qubit pairs in quantum arrays

1.1 Overview on entanglement distribution

The burgeoning availability of quantum computing and communication systems, integrating an increasing number of components, is anticipated to spur a demand for efficient schemes to transfer quantum states or distribute entanglement across networks [1]–[4]. While fundamental protocols for such tasks are established and successfully implemented across various platforms [5]–[13], future quantum devices are expected to necessitate the generation and exchange of entanglement among thousands of qubits within limited coherence times. In response to this, there is a compelling drive to explore quantum communication strategies that are not only fast and parallelizable, but also minimize classical control requirements, moving beyond serial application of existing protocols.

This impetus underlies the recent surge of interest in driven-dissipative quantum systems. One primary objective is to explore how tailored dissipative processes [14], [15] could stabilize entangled quantum states across both few and many-body regimes, potentially impacting quantum information processing [16]–[34]. A seemingly separate avenue of research explores the distinct properties of non-equilibrium steady states emerging in driven quantum spin chains, arising from the interplay of driving, lattice dynamics, and dissipation [35]–[47].

1.2 Introduction

A crucial element in quantum technologies, including quantum computation, simulation, and communication, involves the capability to manage and distribute entangled resources across extensive arrays of quantum systems. A compelling approach employs controlled dissipative processes to steer and protect arrays of quantum systems into entangled states [27], [48]–[56]. Specifically, studies [24], [28], [29],

[31]–[34], [57]–[63] have demonstrated that to drive the whole system into non-trivial and potentially useful multipartite entangled states, it is sufficient to control the dissipative dynamics of one or two localized elements within a quantum array. This has been proved for arrays of both bosonic (by employing a single localized squeezed reservoir [29], [32]–[34], [61]–[63]) and fermionic (via a correlated reservoir for two fermions [28]) modes. Additionally, it has been shown that manipulating the coupling between a central cavity and two qubits (spin-1/2) in a qubit chain [24] and creating a correlated reservoir involving two elements in an array of qubits [28], [31], [57], [60] and cavities (bosonic modes) [31], [57]–[59] can yield many entangled pairs.

Here, we present that, even in the case of qubits, it is enough to control the local environment of a single element within an array to generate many pairs of entangled qubits in the steady state [30]. We establish this for both arrays of cavities and qubits, as well as arrays comprising solely qubits. In the former scenario, a single cavity is coupled to a squeezed reservoir (see to Ref. [64] for an experimental implementation in the microwave domain and Refs. [65], [66] for its application in the optical domain to enhance the performance of gravitational wave interferometers). All interactions in this setup conserve the number of excitations. In the latter case, a single qubit may decay, and the qubits are coupled based on a specific geometry of XY-interactions. We assume, in an ideal scenario, that only one element of the arrays experiences losses. Additionally, we analyze how these dynamics respond to additional noise affecting the qubits.

It is worth noting that similar states have been identified in the ground states of specific spin Hamiltonians [47], [67]–[69], namely the concentric singlet phase [47] and rainbow states [28], [67]. These states can also be induced in a spin chain through specific dynamics [70]–[72], where they are referred to as nested entangled states (or matryoshka states). Moreover, analogous states are recognized as thermofield double states in the high-energy community [73], [74]. Unlike these instances, our findings reveal that these states can exist as the *unique* pure steady state of a dissipative dynamics.

Lastly, we highlight the related findings documented in Refs. [75], [76], although it is important to note that in those cases, the entangled steady states are not unique, so that they are only attained when the system is peculiarly initialized.

The chapter unfolds as follows: In Sec. 1.3, we outline the four models involving both qubits and cavities, elucidating the main outcome — the robust generation of a stationary state featuring many entangled qubit pairs. Moving to Sec. 1.4, we delineate how a comparable dissipative generation of entangled qubit pairs can be achieved with effective models solely involving qubits. In Sec. 1.5, we verify our findings by numerically solving the dynamics of all models introduced in the preceding sections. Finally, Sec. 1.6 is reserved for concluding remarks.

1.3 Models with qubits and cavities

This section delves into the examination of models involving both qubits and cavities. We identify four distinct models distinguished by their geometries and array

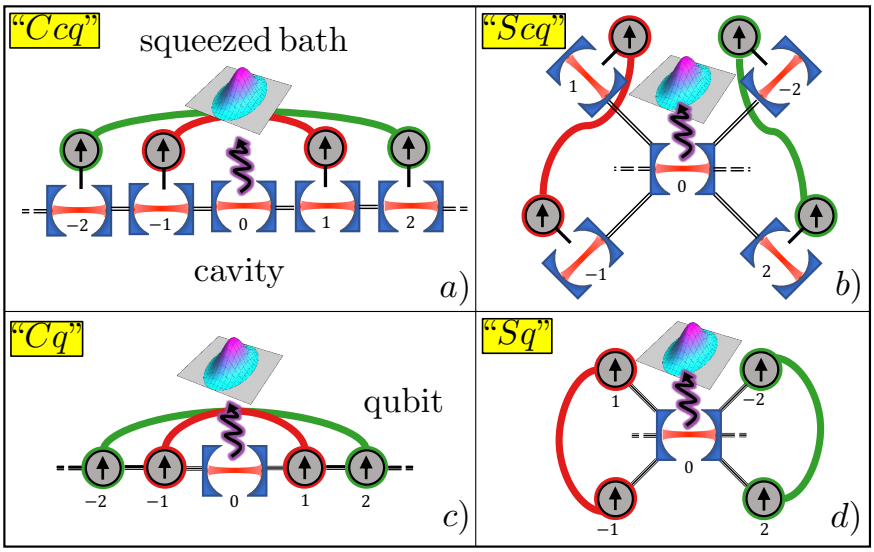

Figure 1.1: (a) Configuration of cavities and qubits denoted as "Ccq", featuring a chain where each cavity, but the central one, interacts with a qubit. The central cavity is locally coupled to a squeezed bath. Irrespective of the initial conditions, steady-state entangled qubit pairs (highlighted by the red and green thick lines) arise. (b) Star-shaped geometry with cavities and qubits "Scq". (c) Chain of qubits with a central cavity "Cq". (d) Star of qubits with a central cavity "Sq".

compositions, outlined as follows. In each scenario, a central cavity is coupled to a squeezed reservoir, resulting in a pure and factorized stationary state between the qubit state $|\psi\rangle$ and the state of the cavity/ies $|\varphi\rangle_c$. Notably, in every instance, each qubit j gets entangled with the $-j$th, giving rise to the formation of many entangled pairs. The steady state of the qubits can be expressed as

$$|\psi\rangle = \bigotimes_{j=1}^{N} \left(\sqrt{\frac{\bar{n}+1}{2\bar{n}+1}} |-\rangle_j |-\rangle_{-j} - \chi_j \sqrt{\frac{\bar{n}}{2\bar{n}+1}} |+\rangle_j |+\rangle_{-j} \right), \tag{1.1}$$

where the variable j runs over all the entangled pairs, N is the total number of pairs (yielding a total of $2N$ qubits), $|\pm\rangle_j$ is the eigenvalue of the Pauli operator $\sigma_j^{(z)}$ for the qubit j, with eigenvalue ± 1, and $\bar{n}$ is the number of excitations in the squeezed reservoir. Moreover, χ_j introduces a phase factor contingent on the specific model [as detailed in Eq. (1.12)]. It is noteworthy that as $\bar{n}$ increases, each pair's state in Eq. (1.1) tends toward a Bell, maximally-entangled state, pivotal in numerous quantum information protocols [77].

1.3.1 The four models

Chain of cavities and qubits. The first model represents an extension of the cavity chain studied in Ref. [29]. In this version, each cavity, but the central one,

interacts also with a qubit [see Fig. 1.1 (a)]. This particular configuration is denoted as "Ccq," where the uppercase "C" signifies a chain, referring to the geometric arrangement, while "cq" the composition of the array, i.e., of cavities and qubits.

Star of cavities and qubits. Likewise, the second model represents an extenstion of a star-like bosonic array, akin to the one examined in Ref. [61]. In this adaptation, each of the external modes interacts with a qubit [refer to Fig. 1.1 (b)]. This particular model is designated as "$S\,cq$," with the "S" denoting the star geometry.

Chain of qubits with a central cavity. Next, we explore a chain of qubits, wherein the central element is, in fact, a cavity (alternatively described as two chains coupled at one end to a shared cavity) [see Fig. 1.1 (c)]. This model is denoted by "Cq," for chain of qubits.

Star of qubits with a central cavity. Lastly, we investigate a star-like array where a central cavity is coupled to many qubits [see Fig. 1.1 (d)]. For this model we use the symbol "$S\,q$."

1.3.2 The master equation

In each scenario, the system dynamics are described by a master equation of the form

$$\dot{\rho} = -\frac{\mathrm{i}}{\hbar}\left[H_{\xi},\, \rho\right] + \frac{\kappa}{2}\mathcal{L}_c\rho, \tag{1.2}$$

with $\xi \in \{Ccq,\, S\,cq,\, Cq,\, S\,q\}$. The Lindblad operator $\mathcal{L}_c$ describes dissipation via the squeezed reservoir of the central cavity with photonic annihilation operator b_0 (see Fig. 1.1), and reads

$$\mathcal{L}_c\rho = \beta_0\rho\beta_0^{\dagger} - \beta_0^{\dagger}\beta_0\rho - \rho\beta_0^{\dagger}\beta_0, \tag{1.3}$$

where

$$\beta_0 = \sqrt{\bar{n}+1}\,b_0 - \sqrt{\bar{n}}\,b_0^{\dagger}, \tag{1.4}$$

is the squeezed annihilation operator. A squeezed reservoir can be achieved by driving the system with a broadband squeezed field [58], [61], [78]. Notably, in the microwave regime, experimental realization of a squeezed reservoir has been reported [64]. This technique has also been employed to enhance the performance of gravitational wave interferometers in the optical domain [65], [66].

1.3.3 The Hamiltonians of the four models

In all instances, we exclusively consider Hamiltonian interactions that conserve the number of excitations. For two interacting cavities with annihilation operators b_j and b_k, our consideration extends to interaction Hamiltonians of the form $H_{c-c} \propto$

$b_j^\dagger b_k + h.c.$ (where $h.c.$ denotes the Hermitian conjugate). Moreover, cavity-qubit interactions are described by Jaynes-Cummings Hamiltonians $H_{c-q} \propto b_j^\dagger \sigma_j + h.c.$, where $\sigma_j = \left[\sigma_j^{(x)} - \mathrm{i}\sigma_j^{(y)}\right]/2$ is the lowering operator for qubit j. Finally, interactions between two qubits are modeled by an XX spin-1/2 Hamiltonian $H_{q-q} \propto \sigma_j^{(x)}\sigma_k^{(x)} + \sigma_j^{(y)}\sigma_k^{(y)} = 2\sigma_j^\dagger \sigma_k + h.c.$.

To be specific, the Hamiltonians corresponding to each of the four models are given in Eqs. (1.5)-(1.8) below. These expressions describe the system in a reference frame rotating at the frequency of the central cavity $\omega_0/2\pi$. In particular, in the models "Ccq" and "Scq" with many cavities (each interacting with a qubit), all qubits are resonant with the central cavity, while the other cavities are detuned by a frequency $\Delta_{c,\,j}$ from ω_0. Conversely, in the models "Cq" and "Sq," consisting of many qubits and a central cavity, the transition frequency of each qubit is detuned by $\Delta_{q,\,j}$ from ω_0. Our analysis relies on the assumption that ω_0 dominates the parameters in the studied systems. As a result, the frequencies of the cavities and qubits ($\omega_0 + \Delta_{c,\,j}$ and $\omega_0 + \Delta_{q,\,j}$, respectively) are orders of magnitude greater than the introduced coupling strengths — a common feature of quantum-optical systems. This crucial assumption justifies our adoption of the local master Eq. (1.2) [79]–[82].

We also note that, for maintaining the steady state Eq. (1.1), the Hamiltonians must adhere to specific symmetry properties: they need to be symmetric in the interaction strengths and antisymmetric in the detunings, as discussed below. This symmetry requirement bears resemblance to the chiral symmetry identified in Ref. [28] (see also Ref. [32]), which underlies the emergence of steady-state entangled pairs — equal to those under investigation here — in a finite chain of qubits when the two central qubits are coupled to a correlated reservoir.

Now, let us explicitly introduce the formulas for the Hamiltonians.

Chain of cavities and qubits: "Ccq" [Fig. 1.1 (a)]

$$\begin{aligned} H_{Ccq} = \hbar \sum_{j=1}^{N} \Big\{ & \Delta_{c,\,j}\left(b_j^\dagger b_j - b_{-j}^\dagger b_{-j}\right) \\ & + \left[g_j\left(b_j^\dagger \sigma_j + b_{-j}^\dagger \sigma_{-j}\right) + \eta_{c,\,j}\left(b_j^\dagger b_{j-1} + b_{-j}^\dagger b_{-j+1}\right) + h.c. \right] \Big\}, \end{aligned} \tag{1.5}$$

where $j = 0$ denotes the central cavity, and positive and negative values of j indicate elements on the right and on the left of the central cavity, respectively, with $|j|$ measuring the distance from the central cavity. Notably, cavities at equal distances on the right and on the left exhibit opposite detunings, while all interactions are symmetric.

In such a situation (and in the following), many entangled pairs form between both qubits and cavities. The dynamics of the cavities align with Ref. [29] (which specializes Ref. [33]). Here, we illustrate how the entanglement within these bosonic modes is transferred to the qubits, similarly to Refs. [16], [31], [57], [83]–[85].

Star of cavities and qubits: "Scq" [Fig. 1.1 (b)]

$$H_{Scq} = \hbar \sum_{j=1}^{N} \left\{ \Delta_{c,j} \left(b_j^\dagger b_j - b_{-j}^\dagger b_{-j} \right) + \left[g_j \left(b_j^\dagger \sigma_j + b_{-j}^\dagger \sigma_{-j} \right) + \eta_{c,j} b_0^\dagger \left(b_j + b_{-j} \right) + h.c. \right] \right\}. \tag{1.6}$$

In this context, the index j no longer indicates the distance from the central cavity; instead, it is employed to label elements entangled in the steady state. In other words, elements (both cavities and qubits) with indices j and $-j$ form entangled pairs. This model shares various features with the previous one. Firstly, the cavities are entangled in the steady state, following a dynamics similar to that in Ref. [33] (see also Ref. [61]), which, in turn, induces entanglement in the qubits, analogous to the previous case [16], [31], [57], [83]–[85]. Secondly, the cavities within each pair have opposite detunings, while their interaction coefficients are equal.

Chain of qubits with a central cavity: "Cq" [Fig. 1.1 (c)]

$$H_{Cq} = \hbar \sum_{j=1}^{N} \frac{\Delta_{q,j}}{2} \left[\sigma_j^{(z)} - \sigma_{-j}^{(z)} \right] + \hbar \left[g_1 b_0^\dagger \left(\sigma_1 + \sigma_{-1} \right) + \sum_{j=2}^{N} \eta_{q,j} \left(\sigma_j^\dagger \sigma_{j-1} + \sigma_{-j}^\dagger \sigma_{-j+1} \right) + h.c. \right], \tag{1.7}$$

where, similar to the "Ccq" model, positive and negative values of j indicate, respectively, the qubits on the right and on the left of the central cavity. A qubit on the right chain has a detuning opposite to that of the corresponding qubit on the left chain, while the corresponding couplings are identical. As described earlier, pairs of qubits at the same distance on the right and on the left of the cavity get entangled in the stationary state.

Star of qubits with a central cavity: "Sq" [Fig. 1.1 (d)]

$$H_{Sq} = \hbar \sum_{j=1}^{N} \left\{ \frac{\Delta_{q,j}}{2} \left[\sigma_j^{(z)} - \sigma_{-j}^{(z)} \right] + \left[g_j b_0^\dagger \left(\sigma_j + \sigma_{-j} \right) + h.c. \right] \right\}. \tag{1.8}$$

As in the "Scq" case, the index j does not indicate the distance from the central cavity, but it is used to label the elements entangled in the steady state, meaning the qubits with indices j and $-j$ form entangled pairs.

1.3.4 The steady state

Let us now examine in detail the steady state of the previously defined models. When $g_j = 0$ (indicating no interaction with the qubits), the squeezed reservoir drives the central cavity towards a squeezed state. Correspondingly, as shown in

Refs. [29], [33], [61], the remaining cavities (in the models "Ccq" and "$S\,cq$") approach a pure entangled state composed of many two-mode squeezed states. This state can be expressed as

$$|\varphi\rangle_c = U_c|0\rangle_c, \tag{1.9}$$

where $|0\rangle_c$ is the vacuum, and U_c the unitary responsible for producing the steady state. In detail, for the cavities and qubits models ("Ccq" and "$S\,cq$"), U_c is the product of a squeezing operator on the central cavity mode and many two-mode squeezing operators for the modes with opposite indices

$$U_c = \mathrm{e}^{\frac{r}{2}\left(b_0^{\dagger 2} - b_0^2\right)} \bigotimes_{j=1}^{N} \mathrm{e}^{\chi_j r\left(b_j^\dagger b_{-j}^\dagger - b_j b_{-j}\right)}, \qquad \text{for } Ccq \text{ and } S\,cq, \tag{1.10}$$

where $\tanh(r) = \sqrt{\overline{n}/\left(\overline{n}+1\right)}$. In contrast for the "$Cq$" and "$S\,q$" models, U_c is the single-mode squeezing operator

$$U_c = \mathrm{e}^{\frac{r}{2}\left(b_0^{\dagger 2} - b_0^2\right)}, \qquad \text{for } Cq \text{ and } S\,q. \tag{1.11}$$

In particular, the term χ_j featured in Eqs. (1.1) and (1.10) is defined as

$$\chi_j = \begin{cases} (-1)^j, & \text{for } Ccq, \\ (-1)^{j+1}, & \text{for } Cq, \\ -1, & \text{for } S\,cq, \\ 1, & \text{for } S\,q \end{cases}, \tag{1.12}$$

for $j \neq 0$. We also note that these operators [Eqs. (1.10) and (1.11)] realize the Bogoliubov transformation

$$U_c^\dagger b_j U_c = \sqrt{\overline{n}+1}\, b_j + \chi_j \sqrt{\overline{n}}\, b_{-j}^\dagger, \tag{1.13}$$

for all j, including $j = 0$ with $\chi_0 = 1$.

Now, it can be verified that, in general, the product state

$$|\Psi\rangle = |\varphi\rangle_c|\psi\rangle, \tag{1.14}$$

involving the qubits state given by Eq. (1.1) and the cavity/ies state given by Eq. (1.9), with U_c and χ_j provided in Eqs. (1.10)-(1.12), *is a steady state for the four models*. In other words, one finds that $-\frac{\mathrm{i}}{\hbar}\left[H_\xi, |\Psi\rangle\langle\Psi|\right] + \frac{\kappa}{2}\mathcal{L}_c\,|\Psi\rangle\langle\Psi| = 0$.

This is the result of the destructive interference occurring when these systems possess the specific symmetries described in Sec. 1.3.3. To elaborate, the Hamiltonians can be separated into distinct components: one involving only the cavity operators $H_{c,\xi}$ (which is non-zero solely for the "Ccq" and "$S\,cq$" models); and the terms describing the interactions between cavity/ies and qubits, denoted as $H_{c-q,\xi}$, such that

$$H_\xi = H_{c,\xi} + H_{q,\xi} + H_{c-q,\xi}, \tag{1.15}$$

we find

$$-\frac{\mathrm{i}}{\hbar}\left[H_{c,\xi},\, |\varphi\rangle_c\langle\varphi|\right] + \frac{\kappa}{2}\mathcal{L}_c\,|\varphi\rangle_c\langle\varphi| = 0, \tag{1.16}$$

as demonstrated in Refs. [29], [32], [33], and

$$\begin{aligned} H_{q,\xi}|\psi\rangle &= 0, \\ H_{c-q,\xi}|\Psi\rangle &= 0, \end{aligned} \tag{1.17}$$

due to the quantum interference that hinders transitions involving qubit states in the quantum superposition Eq. (1.1).

1.3.5 Dynamics in the squeezed representation

To verify Eq. (1.17) and gain insight into the steady-state dynamics, it is useful to analyze the system in a representation where the cavity's steady state corresponds to the vacuum. Namely, we consider the master equation for the transformed density matrix $\widetilde{\rho} = U_c^\dagger \rho U_c$, expressed as

$$\dot{\widetilde{\rho}} = -\frac{\mathrm{i}}{\hbar}\left[\widetilde{H}_\xi, \widetilde{\rho}\right] + \frac{\kappa}{2}\widetilde{\mathcal{L}}_c\widetilde{\rho}, \tag{1.18}$$

with the Lindblad term which describes dissipation of the zeroth mode being

$$\widetilde{\mathcal{L}}_c\widetilde{\rho} = 2b_0\widetilde{\rho}b_0^\dagger - b_0^\dagger b_0\widetilde{\rho} - \widetilde{\rho}b_0^\dagger b_0. \tag{1.19}$$

The transformed Hamiltonian in Eq. (1.18) can be written as

$$\begin{aligned} \widetilde{H}_\xi &= U_c^\dagger H_\xi U_c \\ &= H_{c,\xi} + H_{q,\xi} + \widetilde{H}_{c-q,\xi}, \end{aligned} \tag{1.20}$$

where the Jaynes-Cummings interaction term $\widetilde{H}_{c-q,\xi} = U_c^\dagger H_{c-q,\xi} U_c$ may be expressed as

$$\begin{aligned} \widetilde{H}_{c-q,\xi} &= \hbar\sum_{j=1}^{N} g_j\left(b_j^\dagger\tau_j + b_{-j}^\dagger\tau_{-j} + h.c.\right), \qquad \text{for } \xi \in \{Ccq,\, Scq\}, \\ \widetilde{H}_{c-q,Cq} &= \hbar g_1 b_0^\dagger(\tau_1 + \tau_{-1}) + h.c., \\ \widetilde{H}_{c-q,Sq} &= \hbar\sum_{j=1}^{N} g_j\left[b_0^\dagger\left(\tau_j + \tau_{-j}\right) + h.c.\right], \end{aligned} \tag{1.21}$$

with τ_j given by the collective qubit operator

$$\tau_j = \sqrt{\overline{n}+1}\,\sigma_j + \chi_j\sqrt{\overline{n}}\,\sigma_{-j}^\dagger. \tag{1.22}$$

Now it is straightforward to verify that the transformed state

$$|\widetilde{\Psi}\rangle = \widetilde{|\varphi\rangle}_c|\psi\rangle = |0\rangle_c|\psi\rangle, \tag{1.23}$$

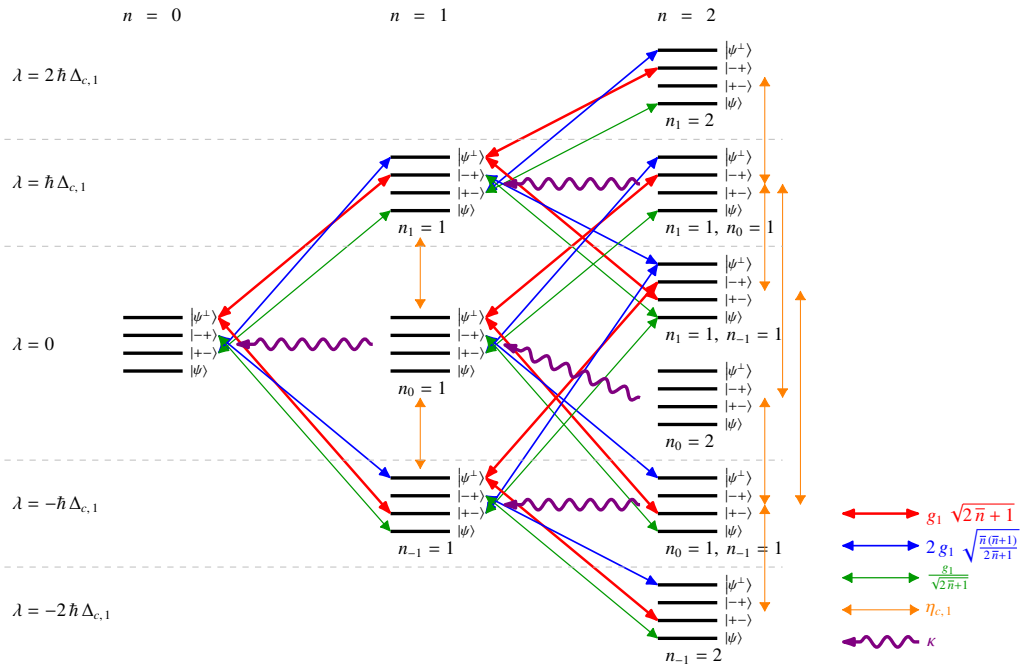

Figure 1.2: Low-excitations eigenlevels (black horizontal lines) for the Hamiltonian $\widetilde{H}_{Ccq}\big|_{\eta_{c,j}=0,g_j=0}$ (in the squeezed representation), excluding interaction terms [see Eqs. (1.5), (1.20) and (1.21)]. The figure includes matrix elements of interaction terms (red, blue, green, and orange arrows; each color marks a different coupling strength, as shown in the right-bottom corner), pertaining to the "Ccq" model with $N = 1$ (equivalent to the "Scq" model with $N = 1$). A purple wavy arrow illustrates population transfer due to the central cavity decay. The qubit state Eq. (1.1) is denoted by $|\psi\rangle = \left(\sqrt{\bar{n}+1}|--\rangle + \sqrt{\bar{n}}|++\rangle\right)/\sqrt{2\bar{n}+1}$ and its orthogonal state by $|\psi^{\perp}\rangle = \left(\sqrt{\bar{n}}|--\rangle - \sqrt{\bar{n}+1}|++\rangle\right)/\sqrt{2\bar{n}+1}$. Parameters n_j and $n \equiv \sum_j n_j$ represent Fock states $|n_{-1}n_0n_1\rangle_c$ of cavities in the squeezed representation (i.e., squeezed Fock states $U_c|n_{-1}n_0n_1\rangle_c$ in the original representation). The values of λ tag the eigenvalues of $\widetilde{H}_{Ccq}\big|_{\eta_{c,j}=0,g_j=0}$ for dirrent group of levels. Horizontal dashed gray lines delineate groups associated with each eigenvalue, and levels with the same eigenvalue (in the same group) are reported at different vertical positions for clarity. The state $|\psi\rangle$ with zero excitations $n = 0$ (steady state) accumulates population, being decoupled from other levels. Indeed, it does not lose population but it is populated by the cavity decay.

(with $\widetilde{|...\rangle} = U_c^{\dagger}|...\rangle$) fulfilling $\widetilde{H}_{c-q,\xi}\,\widetilde{|\Psi\rangle} = 0$ [equivalent to Eq. (1.17)]. Indeed, on one hand, $b_j\widetilde{|\Psi\rangle} = 0$ due to the vacuum state of the cavity/ies (in this representation), and on the other hand

$$\tau_j|\psi\rangle = 0, \qquad \forall\, j. \tag{1.24}$$

In other terms, in this representation, all the cavities dissipate (via the central cavity) and approach the vacuum. Correspondingly, the qubits' population accumulates in the entangled state Eq. (1.1), akin to an optical pumping process. Notably, the

state Eq. (1.23) stands out as the only state that remains unaffected by decay, being decoupled from all others, while concurrently being populated through the decay process of the central cavity.

Illustrating this concept with a straightforward example, let us consider the case when $N = 1$ for the models "Ccq" and "Scq", which are identical. In Fig. 1.2, we report the eigenstates of the system Hamiltonian without interactions, using arrows to connect levels that are coupled by interaction terms. The number of cavity excitations (in the squeezed representation) increases from left to right, and the dissipation of the central cavity induces an irreversible transfer of population from right-side levels to left-side ones. The figure shows that the qubit state Eq. (1.23) [equivalent to the state Eq. (1.1) with zero cavity excitations] is the only state decoupled from the other levels. Simultaneously, it remains immune to decay while being populated through the cavity decay. Consequently, this state maintains stability in the steady state. Analogous considerations apply to the other models as well.

1.4 Models with only qubits

A comparable dynamics of qubits (in the squeezed representation) can be observed by modifying our models to replace all the cavity modes with fresh new qubits. Namely, we may consider the master Eq. (1.18) and substitute all occurrences of b_j and $b_j^\dagger$ with other lowering and rising qubit operators, denoted as $\sigma_{c,j}$ and $\sigma_{c,j}^\dagger$, respectively (where the subscript $_c$ indicates these as the new qubits replacing the cavities from Sec. 1.3 and Fig. 1.1). This transformation yields new models consisting solely of qubits, featuring a single central lossy qubit. Furthermore, the qubits interact with a peculiar structure (unique for each model) of XY-interactions, as depicted in Fig. 1.3.

Let us explicitly express the equations for these models. The master equation takes the form of Eq. (1.18)

$$\dot{\varrho} = -\frac{\mathrm{i}}{\hbar}\left[H_\xi^\circ, \varrho\right] + \frac{\kappa}{2}\mathcal{L}_q\varrho, \tag{1.25}$$

where, also in this case, we continue to employ labels $\xi \in \{Ccq, Scq, Cq, Sq\}$ to highlight the relation with the models in Fig. 1.1, but now the Hamiltonian and the Lindblad operator exclusively include qubit operators, following the substitution $b_j \to \sigma_{c,j}$. In other words

$$\begin{aligned} \mathcal{L}_q &= \widetilde{\mathcal{L}}_c\Big|_{b_j\to\sigma_{c,j}}, \\ H_\xi^\circ &= \widetilde{H}_\xi\Big|_{b_j\to\sigma_{c,j}}, \end{aligned} \tag{1.26}$$

namely

$$\mathcal{L}_q\varrho = 2\sigma_{c,0}\varrho\sigma_{c,0}^\dagger - \sigma_{c,0}^\dagger\sigma_{c,0}\varrho - \varrho\sigma_{c,0}^\dagger\sigma_{c,0}, \tag{1.27}$$

and

$$H_\xi^\circ = H_{c,\xi}^\circ + H_{q,\xi} + H_{c-q,\xi}^\circ, \tag{1.28}$$

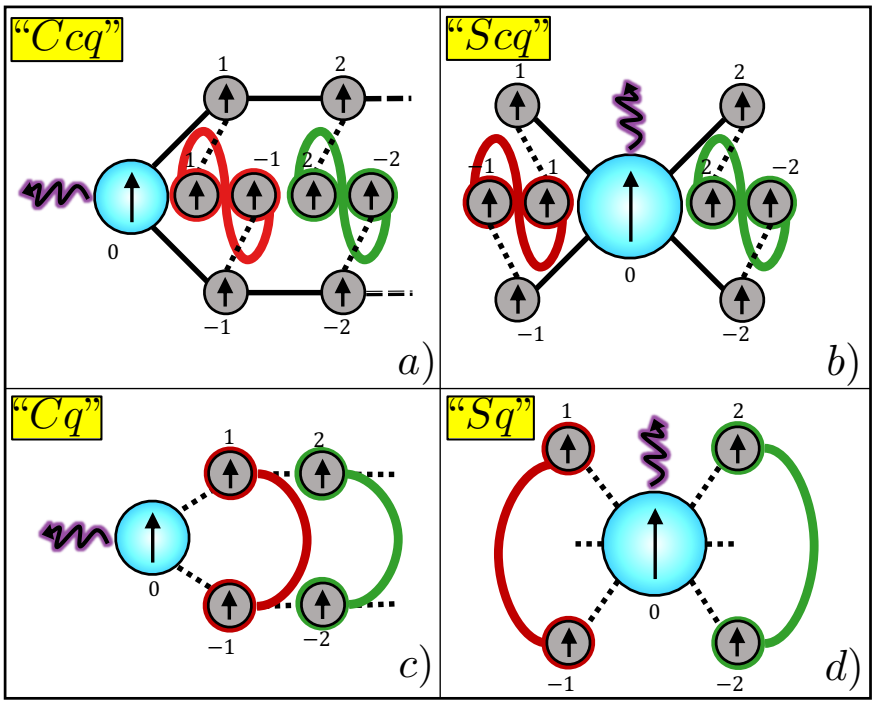

Figure 1.3: Illustration of qubit arrays analogous to the models depicted in Fig. (1.1), with the cavities replaced by additional qubits. Each model features a central lossy qubit (represented by the wavy line), and qubits entangled in the steady state are highlighted by thick red and green lines. In panels (a) and (b), solid black lines connecting two qubits indicate XX- (isotropic XY-) interactions $\propto \sigma_j^{(x)}\sigma_k^{(x)} + \sigma_j^{(y)}\sigma_k^{(y)}$, while dotted black lines represent interactions of the form $\propto \sigma_j^{(x)}\sigma_k^{(x)} - \sigma_j^{(y)}\sigma_k^{(y)}$. For panels (c) and (d), interactions between the central spin and its neighbors are of XY-type, with anisotropic couplings $\propto g^{(x)}\sigma_j^{(x)}\sigma_k^{(x)} + g^{(y)}\sigma_j^{(y)}\sigma_k^{(y)}$. The black lines in (c) connecting the other spins indicate XX-interactions $\propto \sigma_j^{(x)}\sigma_k^{(x)} + \sigma_j^{(y)}\sigma_k^{(y)}$.

where, as in Sec. 1.3, $H_{q,\xi}$ is non-zero only for $\xi \in \{Cq, Sq\}$ and $H^{\circ}_{c,\xi}$ is non-zero only for $\xi \in \{Ccq, Scq\}$, with

$$
\begin{aligned}
H^{\circ}_{c,Ccq} &= \hbar \sum_{j=1}^{N} \sum_{\zeta=\pm} \left[\zeta \Delta_{c,j} \sigma^{(z)}_{c,\zeta j} + \frac{\eta_{c,j}}{2} \left(\sigma^{(x)}_{c,\zeta j}\sigma^{(x)}_{c,\zeta(j-1)} + \sigma^{(y)}_{c,\zeta j}\sigma^{(y)}_{c,\zeta(j-1)} \right) \right], \\
H^{\circ}_{c,Scq} &= \hbar \sum_{j=1}^{N} \sum_{\zeta=\pm} \left[\zeta \Delta_{c,j} \sigma^{(z)}_{c,\zeta j} + \frac{\eta_{c,j}}{2} \left(\sigma^{(x)}_{c,0}\sigma^{(x)}_{c,\zeta j} + \sigma^{(y)}_{c,0}\sigma^{(y)}_{c,\zeta j} \right) \right].
\end{aligned}
\tag{1.29}
$$

Furthermore, the interaction terms, originated from the Jaynes-Cummings terms discussed in the previous section, are expressed as follows: in the models "Ccq" and "Scq," each qubit corresponding to a cavity of the previous model interacts

with two qubits according to the Hamiltonians

$$H^{\circ}_{c-q,\xi} = \hbar \sum_{j=1}^{N} \frac{g_j}{2} \times \sum_{\zeta=\pm} \left\{ \sigma^{(x)}_{c,\zeta j} \left[\sqrt{\bar{n}+1}\,\sigma^{(x)}_{\zeta j} + \chi_j \sqrt{\bar{n}}\,\sigma^{(x)}_{-\zeta j} \right] + \sigma^{(y)}_{c,\zeta j} \left[\sqrt{\bar{n}+1}\,\sigma^{(y)}_{\zeta j} - \chi_j \sqrt{\bar{n}}\,\sigma^{(y)}_{-\zeta j} \right] \right\}, \tag{1.30}$$

for $\xi \in \{Ccq,\ Scq\}$. Conversely, in the models "Cq" and "Sq," the Jaynes-Cummings terms result in the anistrotopic XY-interaction Hamiltonians

$$\begin{aligned} H^{\circ}_{c-q,Cq} &= \hbar \sum_{\zeta=\pm} \left[g^{(x)}_1 \sigma^{(x)}_{c,0} \sigma^{(x)}_{\zeta 1} + g^{(y)}_1 \sigma^{(y)}_{c,0} \sigma^{(y)}_{\zeta 1} \right], \\ H^{\circ}_{c-q,Sq} &= \hbar \sum_{j} \sum_{\zeta=\pm} \left[g^{(x)}_j \sigma^{(x)}_{c,0} \sigma^{(x)}_{\zeta j} + g^{(y)}_j \sigma^{(y)}_{c,0} \sigma^{(y)}_{\zeta j} \right], \end{aligned} \tag{1.31}$$

with

$$\begin{aligned} g^{(x)}_j &= \frac{g_j}{2} \left(\sqrt{\bar{n}+1} + \chi_j \sqrt{\bar{n}} \right), \\ g^{(y)}_j &= \frac{g_j}{2} \left(\sqrt{\bar{n}+1} - \chi_j \sqrt{\bar{n}} \right), \end{aligned} \tag{1.32}$$

where χ_j is defined in Eq. (1.12).

Now, it is straightforward to verify that, as in the previous section, a steady state for these models is given by

$$|\Psi^{\circ}\rangle = |-\rangle_c |\psi\rangle, \tag{1.33}$$

where $|-\rangle_c$ indicates the state for all the qubits with lowering operator $\sigma_{c,j}$, where each qubit is in the eigenstate of $\sigma^{(z)}_{c,j}$ with eigenvalue -1.

1.5 Numerical results

The uniqueness of the steady state Eq. (1.14) can be numerically confirmed for specific choices of the parameters $\Delta_{c,j}$, $\eta_{c,j}$, $\Delta_{q,j}$, $\eta_{q,j}$, and g_j. In this section, we present numerical results obtained in the squeezed representation for different array sizes of the four models introduced in Sec. 1.3. The calculations involve truncating the Hilbert space of the cavities at various Fock numbers. Additionally, we explore the limiting case where the cavity modes are restricted to only two levels, corresponding to the qubit models in Sec. 1.4.

Additionally, we explore the impact of additional noise on these dynamics, as illustrated in Figs. 1.4-1.7, and analyze their scaling behavior with the array size, as shown in Fig. 1.7. We consider Eq. (1.18) and introduce phase noise on the qubits [1].

[1] The effect of extra cavity decay on analogous systems (comprising only cavities) has been extensively investigated in Refs. [29], [33], demonstrating that the entanglement dynamics remains unaffected as long as the overall additional decay rate is smaller than the coupling rate to the squeezed reservoir κ.

This is modeled by the equation $\dot{\widetilde{\rho}} = \widetilde{\mathcal{L}\rho}$, where the total Liouvillian superoperator is given by

$$\widetilde{\mathcal{L}\rho} = -\frac{\mathrm{i}}{\hbar}\left[\widetilde{H}_{\xi}, \widetilde{\rho}\right] + \frac{\kappa}{2}\widetilde{\mathcal{L}_c\rho} + \gamma\widetilde{\mathcal{D}\rho}, \tag{1.34}$$

and where the additional noise on the qubits is described by the Lindblad term

$$\widetilde{\mathcal{D}\rho} = \sum_{\substack{j=-N \\ j\neq 0}}^{N} \sigma_j^{(z)}\widetilde{\rho}\sigma_j^{(z)} - \widetilde{\rho}. \tag{1.35}$$

It is important to note that the structure of the Hamiltonians discussed in the preceding sections is not inherently sufficient to ensure the uniqueness of the steady state. A trivial example is evident in the "Sq" model when all detunings and couplings are equal, such that $\Delta_{q,j} = \Delta_{q,j'}$ and $g_j = g_{j'}$ for all $j, j' \in \{1, \ldots, N\}$. In this highly symmetric scenario, any partition of qubits can be employed to construct a state Eq. (1.1), resulting in a stationary state. Each of these possible partitions will give rise to a stationary subspace in the system dynamics. However, the actual steady state will rely on the initial state and typically manifest as a statistical mixture of states within this subspace. To ensure a unique steady state, such as the pure steady state discussed in Sec. 1.3.4 (or an approximate mixed-state version in the presence of finite γ), it becomes imperative to avoid these highly symmetric situations. One way to achieve this is by employing distinct values of detunings and couplings for each pair.

In this context, we characterize the steady state in terms of the concurrence [77] between pairs of qubits. In particular, we verify numerically that, for the selected parameter set, only qubits with opposite indices j and $-j$ become entangled in the steady state. We numerically compute the system's evolution using wave function Monte Carlo techniques and assess the stability of the results by truncating the Hilbert space of the cavities to various Fock numbers $n_j^{(\max)}$ (refer to Fig. 1.4). To ensure the uniqueness of the steady state in our simulated models, we conduct a numerical analysis on the spectrum of the total Liouvillian. Our findings confirm that, for the given parameters, the steady state is indeed unique, evident from the null space of the Liouvillian having a dimension of one. Due to the numerical complexity of the problem, we focus on small arrays. In the squeezed representation, a relatively low number of Fock states can be employed, with the lowest value $n_j^{(\max)} = 1$ corresponding to models solely featuring qubits (as in Sec. 1.4), while larger values of $n_j^{(\max)}$ approach models that incorporate cavities (as in Sec. 1.3). For models consisting solely of qubits, we can simulate the entire Hilbert space, enabling us to unambiguously demonstrate the uniqueness of the steady state for the chosen parameters. However, in models involving cavities, the simulation is restricted to a finite portion of the infinite-dimensional Hilbert space, raising concerns about the effective uniqueness of the steady state for the complete models. Nonetheless, an examination of Fig. 1.2 suggests that there are no subspaces beyond the simulated part that neither dissipate nor are disconnected from it. This observation implies that the steady state is likely to be unique for these cases as well. In Fig. 1.4 (a)-(c), we observe that in the ideal case ($\gamma = 0$), the steady-state concurrence is the same

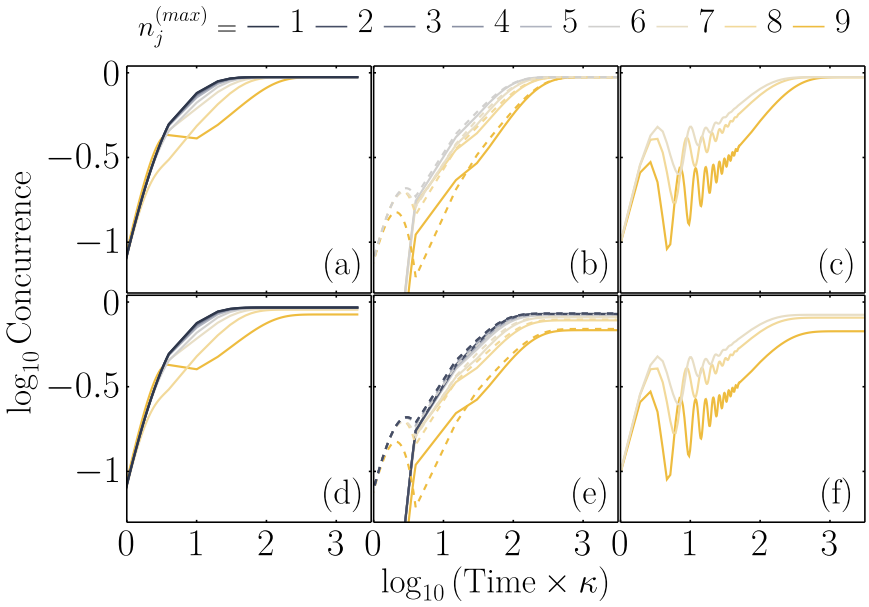

Figure 1.4: Evolution of concurrence over time for different models: "Cq" with a single qubit pair, $N = 1$, in (a) and (d); "Cq" with $N = 2$ in (b) and (e); and "Ccq" with $N = 1$ in (c) and (f). Various values of the dimension of the working Hilbert space of the cavities (in the squeezed representation) are considered, as indicated in the legend. The plots assume $\overline{n} = 1$. In (b) and (e), solid (dashed) lines pertain to the qubit pair $j = 2\,(1)$. In the first row [(a), (b), and (c)], the dephasing rate is $\gamma = 0$. In the second row [(d), (e), and (f)], $\gamma = 5 \times 10^{-4}\kappa$. Specific parameter values include $\Delta_{q,1} \simeq -0.193\kappa$ and $g_1 = 0.36\kappa$ for (a) and (d); $\Delta_{q,1} \simeq -0.193\kappa$, $\Delta_{q,2} = \Delta_{q,1} + 0.05\kappa$, $g_1 = 0.36\kappa$, and $\eta_{q,1} = 0.362\kappa$ for (b) and (e); and for (c) and (f), the Hilbert spaces of all cavities are truncated at the same Fock number $n_0^{(\max)} = n_{\pm1}^{(\max)}$, with $\Delta_{c,1} \simeq -0.26\kappa$ and $g_1 = 0.36\kappa$. The detuning values are chosen to maximize the decay rate of the arrays for the given interaction strengths, selected for simplicity within the same order of magnitude. This is achieved by maximizing the real part of the smallest non-zero value of the total Liouvillian $\mathcal{L}$ as a function of Δ, as illustrated in Fig. 1.5 (c) and Figs. 1.6 (c), (f), and (d) for specific examples.

across all models, irrespective of the dimension of the Hilbert space. This aligns with the findings of Eqs. (1.1) and (1.14), indicating that in the absence of additional dissipation channels, the steady state of the qubits is identical for all models, contingent upon the level of squeezing in the reservoir determined by $\bar{n}$. However, it is noteworthy that the dynamics involving cavities [associated with larger values of $n_j^{(\max)}$] exhibit significantly faster evolution compared to models featuring only qubits [$n_j^{(\max)} = 1$]. Conversely, the presence of dephasing diminishes the final entanglement, with the maximum reduction observed in the slower models, namely those featuring only qubits [refer to Figs. 1.4 (d)-(f)]. Figs. 1.5 and 1.6 illustrate that, under no additional noise ($\gamma = 0$), maximum entanglement is attained for higher values of $\overline{n}$, aligning with the expectation from Eq. (1.1), which approaches

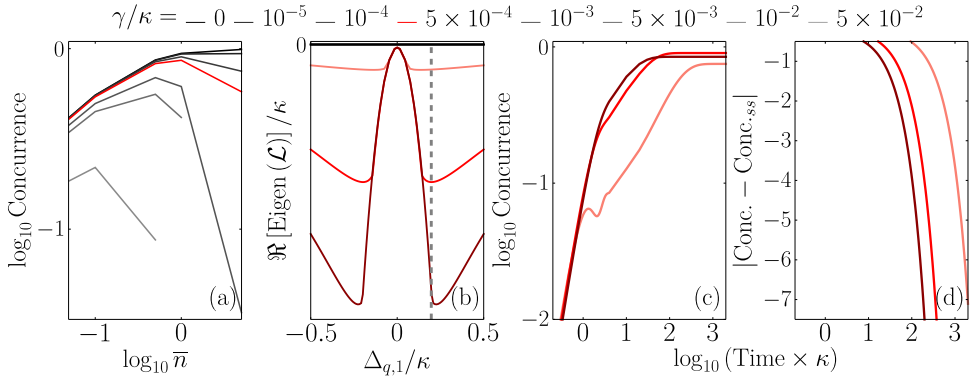

Figure 1.5: (a) Steady-state concurrence for the "Cq" model with $N = 1$ (equivalent to "Sq" with $N = 1$) as a function of the average number of excitations of the squeezed reservoir $\overline{n}$, featuring various values of the dephasing rate γ. (b) Real part of the first two eigenvalues of $\mathcal{L}$ for the same points. The initial state is the vacuum (in the squeezed representation) for the cavity and the eigenstate of $\sigma_j^{(z)}$ with eigenvalue -1 for all the qubits. The vertical black dashed line in (b) indicates the value of $\Delta_{q,1} \simeq 0.197\kappa$. The coupling strength is $g_1 = 0.36\kappa$. The cavity Fock space is truncated at $n_0^{(\max)} = 2$ (in the squeezed representation) to approximate a hybrid model of cavities and qubits. Similar results are confirmed for models of only qubits ($n_0^{(\max)} = 1$) and larger values of $n_0^{(\max)}$. (c) Time evolution of the concurrence for the highlighted (yellow) points in (a), corresponding to $\overline{n} = 0.5$ (dark red), 1 (red), and 5 (salmon) with $\gamma = 5\times10^{-4}\kappa$. (d) Decay rate analysis: same results to (c) where, at each curve, we subtract its steady-state value, take the modulus, and fit the result with an exponential decay. The slopes of these lines indicate the rate of decay towards the steady state. These rates align with the real part of the eigenvalues of $\mathcal{L}$ identified by the vertical dashed line in plot (b).

to the product of many Bell, maximally entangled states. Conversely, in the presence of finite additional noise with a rate γ, maximum entanglement occurs at *finite* values of $\overline{n}$. This is due to the fact that larger $\overline{n}$ leads to slower dynamics, as depicted in these figures [refer to the decay rates for different $\bar{n}$ values in Fig. 1.5 (d)]. Consequently, if γ is excessively large, noise and decoherence have ample time to disrupt the generation of the steady state.

The relationship between a larger $\bar{n}$ and slower dynamics is depicted in Figs. 1.5 (b), (c), and (d) (as well as the corresponding plots in Fig. 1.6). Specifically, in Fig. 1.5 (c) [and Figs. 1.6 (c), (f), and (i)], we report the real part of the eigenvalues of the total Liouvillian $\mathcal{L}$ [see Eq. (1.34)]. The smallest (in modulus) real part determines the rate of decay toward the steady state: a larger (in modulus) real part corresponds to a faster dynamics. This relationship is clearly illustrated in Fig. 1.5 (d), where we depict the time evolution of the concurrence relative to its steady state value. This quantity exhibits an exponential decay with a rate given by the values of the eigenvalues identified in Fig. 1.5 (c). We confirmed this behavior for the other models as well.

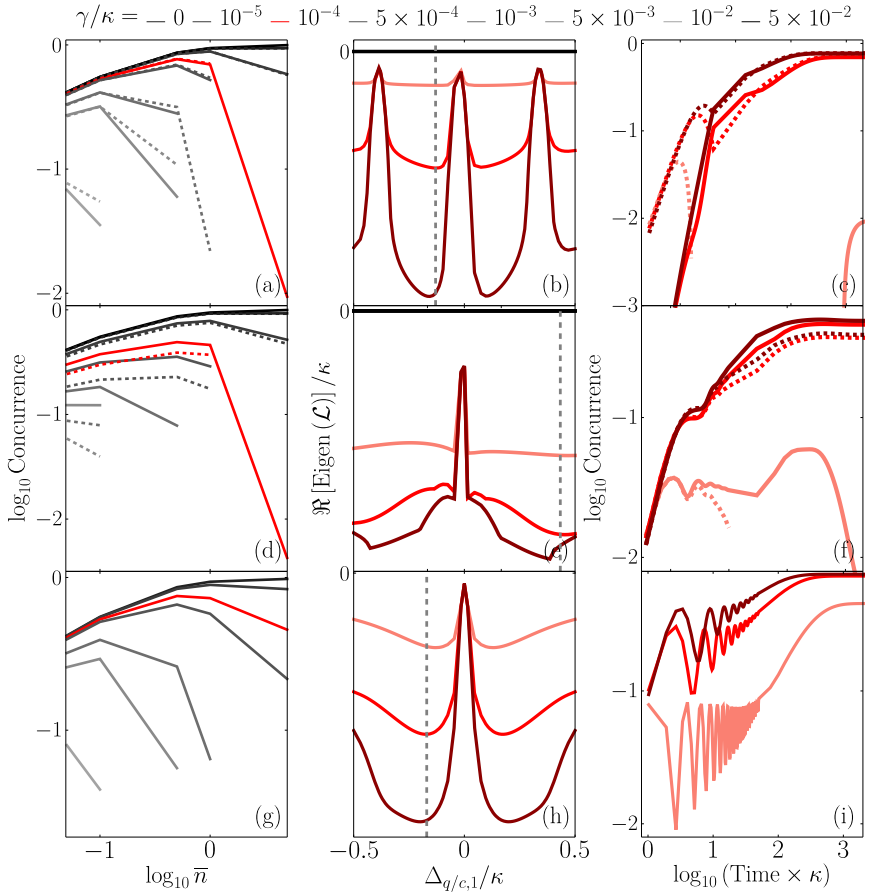

Figure 1.6: Results similar to those in Fig. 1.5 (a)-(c) are presented for the models "Cq" with $N = 2$ (a)-(c), "Sq" with $N = 2$ (d)-(f), and "Ccq" with $N = 1$ (equivalent to "Scq" with $N = 1$) (g)-(i). In (a) and (d), the solid (dashed) lines pertain to the pair $j = 2\,(1)$. For (a)-(c), the parameters are $\Delta_{q,1} \simeq -0.13\kappa$, $\Delta_{q,2} = \Delta_{q,1} + 0.05\kappa$, $g_1 = 0.36\kappa$, and $\eta_{q,1} = 0.362\kappa$. The cavity Fock space is truncated at $n_0^{(\max)} = 2$. In (d)-(f), the parameters are $\Delta_{q,1} \simeq 1.3\kappa$, $\Delta_{q,2} = \Delta_{q,1} + 0.05\kappa$, $g_1 = 0.36\kappa$, and $g_2 = 0.362\kappa$. The cavity Fock space is truncated at $n_0^{(\max)} = 2$. In (g)-(i), the parameters are $g_1 = 0.36\kappa$ and $\Delta_{q,1} \simeq -0.17\kappa$. The Fock spaces of the cavities are truncated at $n_0^{(\max)} = 2$ and $n_{\pm 1}^{(\max)} = 1$.

In Fig. 1.7, we numerically verify that the steady state remains unique even for a larger number of qubit pairs, provided that the values of the detuning and couplings are appropriately selected. We display the concurrence for the model "Cq" with up to 10 qubits. Both the detuning and couplings vary linearly with the pair index according to the relations $\Delta_{q,j} = \Delta^\star + 0.05\kappa(j-1)$ and $\eta_{q,j} = g_1 + 0.002\kappa(j-1)$. In this figure, we maximize the final concurrence as a function of $\Delta^\star$ only. More precisely, we choose the value of $\Delta^\star$ to maximize the smallest real part of the eigenvalues of $\mathcal{L}$ for each N (while keeping all other parameters fixed). This choice determines how quickly the system approaches the steady state, as discussed earlier. These results

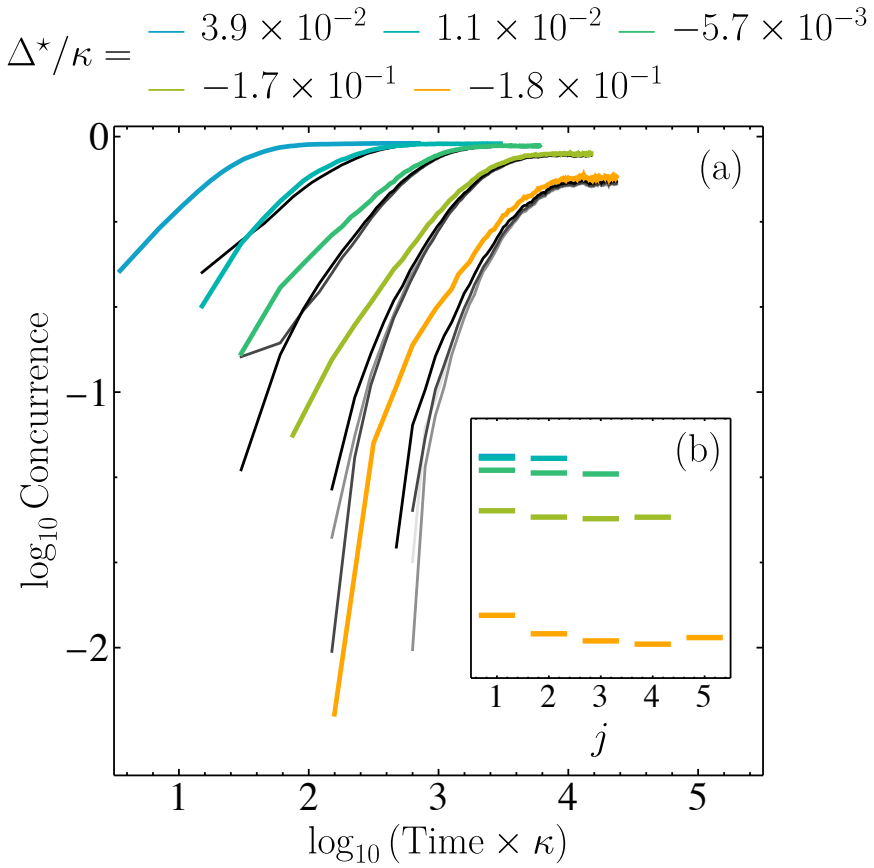

Figure 1.7: (a) Time evolution of the concurrence for the jth pair, considering different numbers of qubit pairs $N \leq 5$ in the "Cq" model. $N = 1$ is denoted in cerulean, $N = 2$ in turquoise, $N = 3$ in sea green, $N = 4$ in lime green, and $N = 5$ in amber. Only the results for the first pair are color-coded, while all others are presented in grayscale. The Fock space of the central cavity is truncated at $n_0^{(\max)} = 2$. System parameters include $g_1 = 0.36\kappa$, $\eta_{q,j} = g_1 + 0.002\kappa(j-1)$, and $\Delta_{q,j} = \Delta^\star + 0.05\kappa(j-1)$, where the value of $\Delta^\star$ is distinct for each N as indicated in the legend, chosen to maximize the concurrence. (b) Corresponding steady-state concurrence for all pairs.

demonstrate that the final concurrence decreases with the number of pairs and exhibits a behavior closely resembling the entanglement obtained in chains of bosonic modes [29]. Finally, we examine, in Figs. 1.8 and 1.9, the impact of random variations in the system parameters from the symmetric configurations identified in Secs. 1.3 and 1.4. The findings indicate that, as expected, the entanglement in the steady state tends to decrease when the system lacks symmetry. The reduction is more noticeable for deviations in the values of the detunings than in the couplings and becomes more pronounced with an increase in system size.

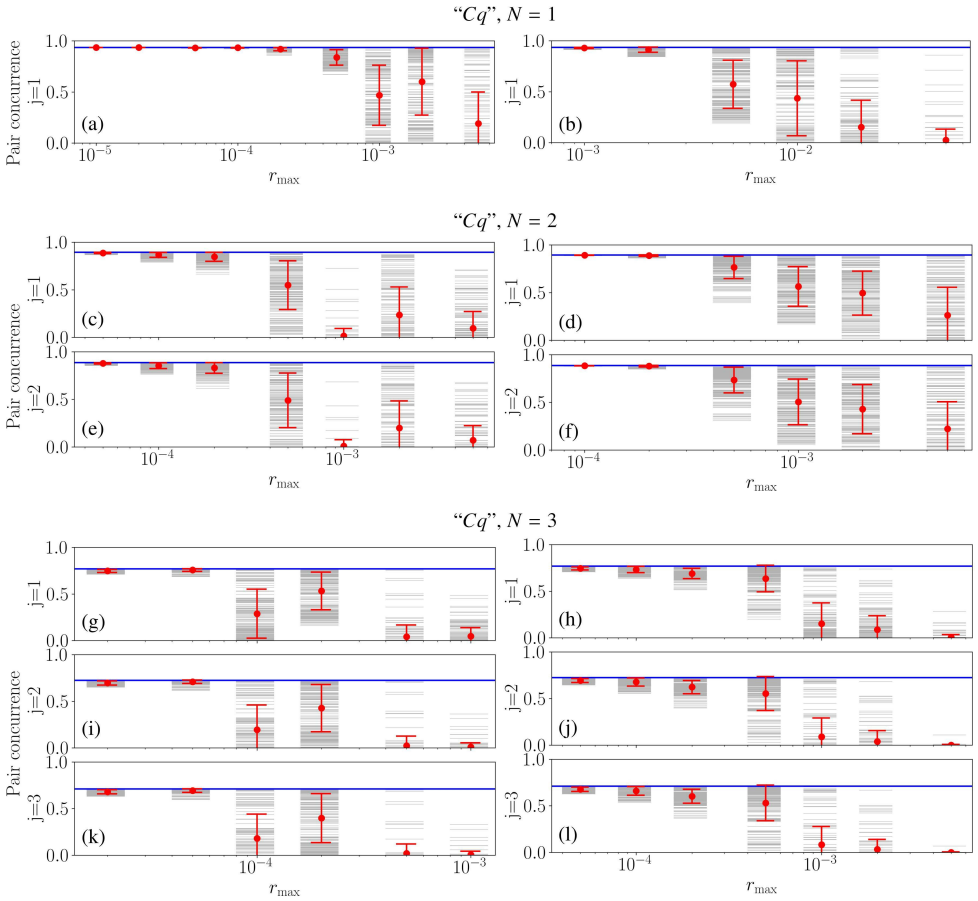

Figure 1.8: Steady state concurrence for the "Cq" model comprising only qubits with $N = 1$, 2, and 3 entangled pairs, evaluated under random variations of the system parameters from the symmetric configuration used in the previous figures. The results in the left column are obtained by relaxing the condition of opposite detunings for qubits with opposite indices. Instead of $\Delta_{q,j}$, we use $\Delta^{(r)}_{q,\pm j} = \pm\Delta_{q,j}\left(1 + r^{(\Delta)}_{\pm j}\right)$, where $r^{(\Delta)}_{\pm j}$ are random variables uniformly distributed in the range $[-r_{\max}, r_{\max}]$. The results in the right column are obtained by relaxing the condition of equal couplings for qubits with opposite indices. Instead of g_1 and η_j, we use $g^{(r)}_{\pm 1} = g_1\left(1 + r^{(g)}_{\pm j}\right)$ and $\eta^{(r)}_{\pm j} = \eta_j\left(1 + r^{(\eta)}_{\pm j}\right)$, respectively, with $r^{(g)}_{\pm 1}$ and $r^{(\eta)}_{\pm j}$ being random variables uniformly distributed in the range $[-r_{\max}, r_{\max}]$. In each plot, for each value of $r_{\max}$, we present 200 random realizations (gray lines), their corresponding averages (red dots), and standard deviations (red lines). The blue lines represent the ideal results evaluated for the symmetric configuration with $r^{(\Delta)}_j = r^{(g)}_j = r^{(\eta)}_j = 0$. All plots share the parameters $\Delta_j = (1.8 + 0.2\,j)\,\kappa$, $g_1 = 0.3\,\kappa$, $\eta_j = (0.45 + 0.05\,j)\,\kappa$, and $\gamma = 10^{-5}\kappa$.

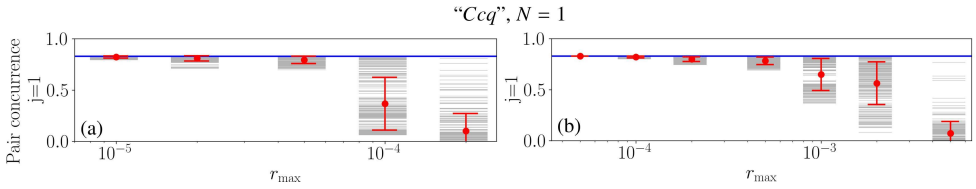

Figure 1.9: As in Fig. 1.8 (a) and (b) for the model "*Ccq*" with only qubits.

1.6 Conclusions

We have shown the feasibility of driving a quantum array into a pure steady state featuring many entangled qubit pairs. This control is achieved by manipulating the dissipative dynamics of a single central element, be it a cavity or a qubit. The purity of the steady state is maintained when dissipation acts solely on the central element. However, in the presence of additional decoherence affecting other qubits, the stationary state becomes an entangled mixed state. Notably, its entanglement remains substantial and resilient, especially when the decay rate of the supplementary dephasing processes is significantly smaller than that of the dissipative decay rate of the central element.

These models have broad applicability and can be implemented in various physical scenarios involving atomic systems [86]–[90] and solid-state nano-devices [91]–[103]. This flexibility allows for the realization of both chain and star geometries.

An intriguing extension of this work involves exploring whether similar approaches can be employed for the preparation of more intricate multipartite entangled qubit states, such as the graph states essential for measurement-based quantum computers [104]. Analogous achievements have been demonstrated for bosonic modes in Ref. [33].

Chapter 2

Microwave quantum illumination with correlation-to-displacement conversion

2.1 Overview on Quantum Illumination

Quantum illumination (QI) marks the forefront of emerging technology, harnessing entangled states to surpass classical benchmarks. Originating from preliminary studies in 2005 that illuminated entanglement's potential to enhance discernibility of entanglement-breaking channels [105], the QI protocol was subsequently introduced in 2008 [106], [107]. Employing an entanglement-based strategy, this protocol enhances detection capabilities of weakly-reflecting objects amidst bright thermal backgrounds. Its enduring significance is evidenced by replication across various contexts. Essentially, a source generates entangled pairs, with one member probing the target region while the other awaits recombination with the signal upon its return. Optimal joint measurement of this pair exploits their entangled nature, yielding heightened sensitivity to the target detection challenge.

Initially confined to the optical domain, QI models spanned both discrete- [106] and continuous-variable [107] systems, representing an initial extension of classical LiDAR (Light Detection and Ranging) into the quantum realm. However, insights from these early endeavors unveiled the potential of non-optical frequencies, particularly in environments characterized by intense thermal noise. Consequently, in 2015, the QI paradigm shifted to the microwave regime [108], where amplified background noise enhances its quantum advantage. This transition marked the inception of the first theoretical blueprint for quantum radar, poised to outperform classical designs in efficacy.

The foundational principles underpinning sensitivity enhancement in QI protocols, in contrast to classical counterparts, are firmly rooted in the framework of quantum detection and estimation theory introduced by Helstrom [109]. This theory, based on quantum hypothesis testing, deduces the optimal measurement operator to minimize error probabilities associated with single-copy discrimination of

quantum states. It extends and generalizes Chernoff's theory [110], holding particular relevance within the domain of quantum discrimination.

Despite successful experimental demonstrations of various QI protocols, spanning optical [111]–[114] to emerging microwave applications [115]–[118], the realization of a functional quantum radar, particularly one based on entanglement, faces formidable technological hurdles. Notwithstanding excitement within defense circles and the media regarding the military applications of quantum radars, the tangible prospect of a fully-fledged quantum radar, capable of sustaining quantum advantage across substantial distances in practical scenarios, remains elusive.

Indeed, the journey toward a quantum radar is fraught with myriad challenges, both theoretical and experimental, hampering the fulfillment of essential criteria. Notably, fully quantum designs, reliant on entanglement distribution akin to QI and joint quantum measurements, prove susceptible to losses, hindering practical implementation in microwave scenarios. At optical frequencies, the pervasive high-noise environment typical of atmospheric conditions is not consistently met. Moreover, issues such as signal fading impose additional constraints on exploiting sensitivity advantages in realistic scenarios [119]. In the microwave frequency domain, two primary hurdles hinder quantum radar development. Firstly, achieving extremely low signal intensities necessary for quantum illumination, as opposed to coherent light, poses a significant challenge. Secondly, attaining the ultra-low temperatures required to generate entanglement remains a formidable obstacle. In the context of accuracy enhancement applications, requisite integration times present a major practical challenge. Consequently, near-term development of a long-range quantum radar appears improbable. Additionally, aside from distance constraints, formidable hurdles loom concerning ranging capabilities and detection times.

However, despite the long road ahead for quantum radar development, the application of QI holds promise for short-range detection of stationary or slow-moving targets, as for example in scanning and surveillance scenarios. In this case, in fact, ranging is not relevant, and the interrogation time can be long enough. The inherent advantage of the quantum design lies in reducing error probabilities while minimizing the mean number of photons necessary for scanning. Moreover, the latter feature of very low irradiation energies, makes QI also potentially useful for biomedical scanning applications.

2.2 Introduction

Quantum illumination is an entanglement-assisted sensing scheme that enhances the precision and sensitivity of target detection [106], [107], [120], [121], via entangling the signal probes with locally stored idlers. Originally developed to simply detect the presence or absence of a target, QI offers a 6-decibel improvement in error exponent due to entanglement [107]. In recent years, QI has been extended to improve target range and angle detection [122], [123], demonstrating an even greater advantage over classical counterparts in the intermediate signal-to-noise-ratio (SNR) region, thanks to the threshold phenomena of nonlinear parameter estimation [123].

Despite these theoretical advancements in QI, its experimental realization in

the microwave domain, which is the natural scenario for its application, has faced several limitations. One of the practical challenges is the need for extensive cooling for microwave quantum-limited detection, due to the high natural noise background, and the lack of developed photon-counting detection technology [118], [124]. To address these issues, a solution for QI based on optical-microwave transduction has been proposed [108]. This approach utilizes an optical idler mode for noiseless storage at room temperature, and up-converts the microwave return mode to the optical domain for quantum-limited joint detection of optical photons. However, the current state-of-the-art efficiency in optical-microwave transduction [4], [13], [125]–[128] falls short of what is required to sustain this transduction-based scheme in the near future.

In addition to the practical challenges, a fundamental limitation of QI is the receiver design problem. Currently, practical receivers such as the optical parametric amplifier receiver (OPAR) and the phase-conjugate receiver (PCR) can only attain half of the error exponent advantage [129]. The optimal receiver would require unit-efficiency sum-frequency-generation at the single photon level [130], which is highly challenging to realize experimentally. The problem of optimal receiver design seems to necessitate nonlinear processes and joint operations on the idler and return modes, making it difficult to implement in practice.

Previous in-principle demonstrations of QI target detection have been hindered by the aforementioned limitations. One example is an optical domain simulation, which injected noise to mimic a microwave scenario and utilized a sub-optimal OPAR [113]. This approach achieved approximately 20% of the error exponent advantage. Another demonstration in the microwave domain used a digitally reconstructed PCR [117], but was unable to surpass the performance of the classical benchmark represented by an ideal coherent state source with the same mean number of photons and homodyne detection. More recently, the OPAR scheme was adapted to the microwave domain, overcoming several challenges in microwave photon processing [118] and again yielding roughly 20% of the error exponent advantage.

A recent development in the field of optimal receiver design is the correlation-to-displacement ('C→D') conversion proposal, which suggests that the optimal receiver design can be achieved by heterodyne-detecting the return mode separately and processing the associated conditional idler field [131]. Upon heterodyne detection of the return modes, the idler modes collapse to coherent states embedded in weak thermal noise. With the help of well-established coherent state discrimination protocols, the C→D receiver design can attain the optimal error probability of QI [132]. This receiver design requires only programmable linear optics [133], [134] and photon detection, making it more feasible for experimental realization. Additionally, it eliminates the need for mode-matching between the noisy return fields at room temperature and the cooled idler fields, avoiding technical difficulties. In this study, we evaluate the feasibility of the C→D receiver design in the microwave domain [135]. We account the lossy antenna coupling to the detection in real radar systems, by introducing loss $1 - \eta_S \leq 1$ in the return mode prior to heterodyne detection. To mitigate this loss, we suggest using parametric amplification with gain $G \geq 1$. Our

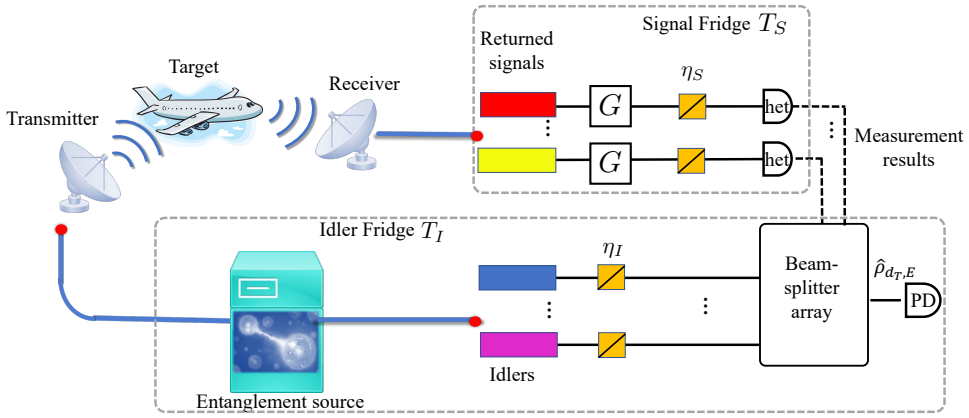

Figure 2.1: Schematic of quantum illumination, with a practical receiver based on correlation-to-displacement conversion, in the presence of noise and loss. A set of M signal-idler TMSV states is generated by an entanglement source, with the idler mode (a_I) stored in a refrigerator (at temperature T_I) for later detection. The signal mode (a_S) is transmitted from the transmitter to investigate a target, which is represented by a phase-shift thermal-loss channel ($\Phi_{\kappa,\theta}$). The returning modes (a_R) are gathered at the receiver, where they undergo processing (at temperature T_S). To account for losses (η_S) and noise, they are first amplified (G) before being heterodyne-detected (het). The measurement results are then collected and used to operate a programmable beamsplitter array. This array transforms the phase-sensitive cross-correlation among the M signal-idler pairs into the complex displacement amplitude d_T of a collective idler mode (with thermal photon number E) at the output of the array, which is detected by a photodetector (PD). We take into account the impact of imperfect idler detection using the η_I elements, which commute with the beamsplitter array and thus appear beforehand.

results show that the full optimal six-decibel error-exponent advantage can be retained when $G\eta_S \gg 1$ if the amplifier is quantum limited. Even if the amplifier introduces noise at room temperature, the C→D receiver still provides a three-decibel advantage over the ideal classical system. Furthermore, we consider the case of limited detection capability in the idler modes. Instead of the complex Dolinar receiver, we consider the simpler Kennedy receiver and still observe the optimal error exponent advantage. Finally, we compare the practical C→D receiver design with both the classical coherent-state homodyne detection and the PCR (which is more effective than the OPAR [136]).

This chapter is organized as follows. Sec. 2.3 describes the protocol, while Sec. 2.4 recalls the basic properties and tools of QI. Sec. 2.5 provides a brief review of the C→D receiver and its performance under ideal conditions. Sec. 2.6 discusses relevant experimental limitations in the case of microwave QI, and Sec. 2.7 shows the performance of the C→D module in the presence of such realistic scenarios. Sec. 2.8 compares the performance of the C→D module with that of classical QI based on coherent state and homodyne detection and that of the PCR. In Sec. 2.9, we consider performance enhancement if we further allow number-resolving detection. In particular, Sec. 2.9.2 presents the Neyman-Pearson framework and receiver operating characteristic (ROC) curves. Finally, we conclude in Sec. 2.10.

2.3 Overall protocol

As shown in Fig. 2.1, in a target detection scenario, the transmitter sends signals to the target, and then the receiver collects return signals and performs measurement to infer about target's presence or absence. To benefit from entanglement, a source generates pairs of idler-signal entangled pulses. The idlers are stored locally and used to assist joint measurements with the return signals. In QI, such signal-idler entanglement provides a six-decibel error exponent advantage, despite being destroyed by extremely lossy transmission and high noise background.

Our proposed receiver system adapts the C→D conversion approach to practical receiver operating conditions. While the idlers are cooled to $T_I \sim 10$ mK to enable quantum advantage, the returned signal part is cooled to a much higher temperature T_S for experimental convenience. Such a layout is possible as the C→D conversion module only feeds the classical heterodyne measurement results on the "warm" and noisy returned signals, to perform conditional linear optical transforms on the "cool" idler alone (indicated by the dashed line), avoiding idler contamination. Finally, photo-detection is performed on the transformed idler, and a decision on the target's presence or absence is made according to the measurement result. To compensate for additional loss $1 - \eta_S$ at the receiver antenna, amplification of gain G is performed. On the contrary, the loss $1 - \eta_I$ on the idler needs to be minimized and cannot be compensated. In fact, the idler pulses are not contaminated by noise, and any amplification will actually degrade the overall performance. The photo-detection can be realized via coupling the microwave idler modes to transmon qubits, as demonstrated in Refs. [118], [124].

2.4 Quantum illumination for target detection

QI is a quantum-based remote sensing technique that leverages the entanglement between signal (a_S) and idler (a_I) modes. The signal mode probes a target region, while the idler one is kept at the emission station. By performing a joint measurement on the signal and idler modes, the quantum correlations of the transmitted state are exploited at the receiving station. The problem is framed as a binary decision-making task, where the two hypotheses are: "target absent" (H_0) and "target present" (H_1). The asymptotic optimal input state is a two-mode squeezed vacuum (TMSV) state, a bipartite Gaussian state characterized by its covariance matrix (CM) [132], [137]

$$\mathbf{V}_{SI} = \begin{pmatrix} (2N_S + 1)\,\mathbf{I} & 2\sqrt{N_S\,(N_S + 1)}\mathbf{Z} \\ 2\sqrt{N_S\,(N_S + 1)}\mathbf{Z} & 2\,(N_S + 1)\,\mathbf{I} \end{pmatrix}, \tag{2.1}$$

where $\mathbf{Z} = \mathrm{diag}\{1, -1\}$, $\mathbf{I} = \mathrm{diag}\{1, 1\}$, and $\left\langle a_S^\dagger a_S \right\rangle = N_S$ is the signal brightness. While the idler is stored for later detection, the signal is transmitted through a phase-shift thermal-loss channel $\Phi_{\kappa,\theta}$, whose action on its mode when the target is present is described by

$$a_R = \mathrm{e}^{\mathrm{i}\theta}\sqrt{\kappa}a_S + \sqrt{1-\kappa}a_B, \tag{2.2}$$

while the absence of a target corresponds to the case $\kappa = 0$, i.e., where the channel is $\Phi_{0,0}$. Upon the channel $\Phi_{\kappa,\theta}$, the CM Eq. (2.1) becomes

$$\mathbf{V}_{RI} = \begin{pmatrix} [2\,(\kappa N_S + N_B) + 1]\,\mathbf{I} & 2\sqrt{\kappa N_S\,(N_S + 1)}\mathbf{R}\mathbf{Z} \\ 2\sqrt{\kappa N_S\,(N_S + 1)}\mathbf{Z}\mathbf{R}^T & (2N_S + 1)\,\mathbf{I} \end{pmatrix}, \tag{2.3}$$

where $\mathbf{R} = \cos\theta\mathbf{I} - \mathrm{i}\sin\theta\mathbf{Y}$ (with $\mathbf{Y}$ indicating the Pauli-Y matrix) and $\left\langle a_B^\dagger a_B \right\rangle = N_B/(1-\kappa)$ is the mean number of thermal background photons. Tab. 2.1 shows the mean thermal photon number for a typical microwave field at $\omega = 2\pi \times 5$ GHz at temperatures of interest. The signal and return modes propagate at room temperature, while — depending upon the chosen device — detectors and amplifiers can be operated at temperature T_S equaling either the room temperature, a few Kelvins, or ideally close to the Josephson parametric amplifier generating the TMSV state at microwave frequency [138], [139], which is typically placed in the cold plate of a dilution refrigerator at about 10 mK [115], [117], [118]. The idler is always stored in the dilution refrigerator at about $T_I \sim 10$ mK [115], [117], [118], to enable quantum advantages.

2.5 Correlation-to-displacement conversion in the ideal case

Ref. [131] proposes a conversion module for capturing and transforming quantum correlation into coherent quadrature displacement, to enable the optimal receiver design for various entanglement-enhanced protocols. The module is based on heterodyne and programmable passive linear optics, and maps the multi-mode quantum detection problem to the semi-classical detection problem of a single-mode noisy

$\omega/2\pi$ [GHz]	T [K]	$N \sim$
5	3×10^2	1.25×10^3
	10^2	4.15×10^2
	10	40
	4	15
	1	4
	10^{-1}	10^{-1}
	10^{-2}	4×10^{-11}
	4×10^{-3}	9×10^{-27}

Table 2.1: Values of mean thermal photon numbers for a microwave mode at $\omega = 2\pi \times 5$ GHz at temperature values of interest.

coherent state, allowing for explicit measurements to achieve the optimal performance. The module provides a paradigm for processing noisy quantum correlations for near-term implementation and can be applied to a wide range of entanglement-enhanced protocols, including quantum illumination, phase estimation, classical communication, target ranging, and thermal-loss channel pattern classification.

QI for target detection considers the discrimination between two channels, $\Phi_{0,0}$ and $\Phi_{\kappa,0}$. In fact, we will consider from now on the simple case of a fixed known phase-shift θ (which can always be chosen equal to zero), as the protocol's performance in the large M limit is independent of this phase [123]. Additionally, the possibility of a random return phase-shift has been explored [140].

In the ideal case, the conversion module produces the displaced thermal states ρ_{0,N_S} (target absent, H_0) and $\rho_{\sqrt{x},E}$ (target present, H_1), where

$$\rho_{\alpha,E} = \sum_{n=0}^{+\infty} \frac{E^n}{(E+1)^{n+1}} D(\alpha) |n\rangle\langle n| D^\dagger(\alpha), \tag{2.4}$$

with $|n\rangle$ a Fock state and $D(\alpha)$ the displacement operator. The total displacement amplitude square $x \sim P^{(M)}(\cdot\,; \xi_{\text{Ideal}})$ obeys a (generalized) χ^2 distribution with $\xi_{\text{Ideal}} \equiv \kappa N_S(N_S+1)/2(\kappa N_S + N_B + 1)$. Here the probability density function for the χ^2 distribution parameterized by ξ is given by

$$P^{(M)}(x;\, \xi) = \frac{x^{M-1} \mathrm{e}^{-x/(2\xi)}}{(2\xi)^M \Gamma(M)}, \tag{2.5}$$

where $\Gamma(M) = (M-1)!$ is the gamma function [131]. This leads to the error probability performance limit

$$P_{\text{C}\not\to\text{D}} = \int_0^{+\infty} dx\, P^{(M)}(x;\, \xi)\, P_{\text{H}}\left(\rho_{0,N_S}, \rho_{\sqrt{x},E}\right), \tag{2.6}$$

where P_{H} is the Helstrom limit [109], [141], [142]

$$P_{\text{H}}(\rho_1, \rho_2) = \frac{1}{2}\left(1 - \frac{1}{2}\text{Tr}\left[|\rho_1 - \rho_2|\right]\right), \tag{2.7}$$

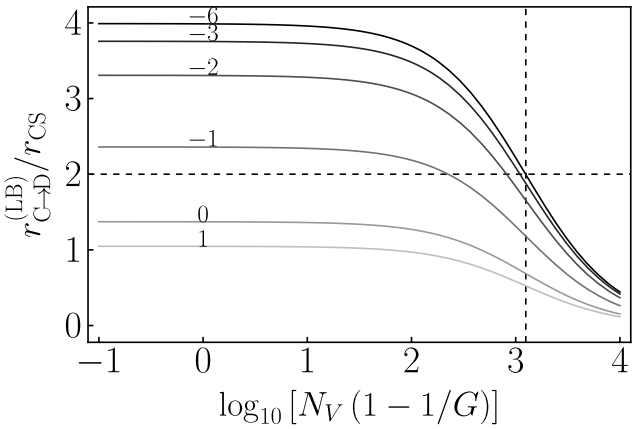

Figure 2.2: Behavior of $r^{(\mathrm{LB})}_{\mathrm{C}\to\mathrm{D}}/r_{\mathrm{CS}}$ as a function of $\log_{10}[N_V(1-1/G)]$ with amplification and ideal signal and idler detection, for different values of $\log_{10} N_S$, given $N_B = 1250$ and $\kappa = 0.01$. $N_S = \left\{10^1, 10^0, 10^{-1}, 10^{-2}, 10^{-3}, 10^{-6}\right\}$ from bottom to top, as indicated by the labels on top of the curves. The plot indicates that the amplification stage provides a factor of advantage greater than 2 (as indicated by the horizontal dashed line) for a range of relevant parameters. This is due to the robust compensation of noise effects achieved by amplifying, as demonstrated by the vertical dashed line at $N_V(1-1/G) = N_B$.

in the case of equal prior probability. As shown in Ref. [131], even though the exact solution of Eq. (2.6) is challenging, we can obtain lower (LB) and upper bounds (UB) for the error exponent $r_{\mathrm{C}\to\mathrm{D}} = -\lim_{M\to\infty} \ln(P_{\mathrm{C}\to\mathrm{D}})/M$. The upper bound can be achieved by approximating $\rho_{\sqrt{x},E}$ as a coherent state and ρ_{0,N_S} as vacuum. In the respect of the asymptotic analysis, the Helstrom limit approaches $P_{\mathrm{H}}\left(\rho_{0,N_S}, \rho_{\sqrt{x},E}\right) \sim \mathrm{e}^{-x}/4$, which — combined with Eq. (2.6) — gives the upper bound $r^{(\mathrm{UB})}_{\mathrm{C}\to\mathrm{D}} = 2\xi$. On the other hand, a lower bound of the conversion module performance can also be obtained as [131]

$$r^{(\mathrm{LB})}_{\mathrm{C}\to\mathrm{D}} = 2\xi\left(\sqrt{N_S+1} - \sqrt{N_S}\right)^2. \tag{2.8}$$

In comparison, the optimal classical case, achieved when a coherent-state with mean photon number N_S is sent to the target, has the error exponent

$$r_{\mathrm{CS}} = \kappa N_S\left(\sqrt{N_B+1} - \sqrt{N_B}\right)^2. \tag{2.9}$$

In the $N_S \ll 1$ and $N_B \gg 1$ limit, one finds that $r^{(\mathrm{UB})}_{\mathrm{C}\to\mathrm{D}} \simeq r^{(\mathrm{LB})}_{\mathrm{C}\to\mathrm{D}} \simeq 4r_{\mathrm{CS}}$, which achieves the optimal advantage.

2.6 Practical microwave detection scenario

Regardless of the technology or setup employed, non-idealities or imperfections will always exist in practical systems, affecting their performance. To mitigate this, we

propose the use of a pre-detection amplifier, which can compensate for additional coupling loss. Our results demonstrate that this approach can effectively improve the performance of binary hypothesis testing and enhance the accuracy of state discrimination.

Before detection, the returned mode is amplified using a quantum amplifier, leading to the amplified mode

$$a_A = \sqrt{G}a_R + \sqrt{G-1}a_V^\dagger, \tag{2.10}$$

where $\left\langle a_V^\dagger a_V \right\rangle = N_V$ is the mean photon number of the amplifier noise mode. The amplified a_A and the idler a_I modes share the CM

$$\mathbf{V}_{AI} = \begin{pmatrix} (2N_A+1)\,\mathbf{I} & V_{12}\mathbf{RZ} \\ V_{12}\mathbf{ZR}^T & (2N_S+1)\,\mathbf{I} \end{pmatrix}, \tag{2.11}$$

where

$$\begin{aligned} N_A &= \left\langle a_A^\dagger a_A \right\rangle \\ &= G\left[\kappa N_S + N_B + (1-1/G)\,(N_V+1)\right], \\ V_{12} &= 2\sqrt{G\kappa N_S\,(N_S+1)}. \end{aligned} \tag{2.12}$$

Microwave amplifiers with gain $G \sim 100$ and excess noise of $N_V \sim 10$ photons have been successfully utilized in various microwave QI experiments [117]. Additionally, superconducting quantum computers employ microwave quantum-limited amplifiers that exhibit added noise levels of about half a photon [143]. The behavior of such experimental systems can be accurately described by the phase-insensitive linear amplifier model presented in Eq. (2.10).

It should be noted how, comparing Eq. (2.11) with the one without any amplification Eq. (2.3), the performance lower bound Eq. (2.8) applies also to the case with the amplifier, as long as one replaces the parameters $\kappa \to G\kappa$ and $N_B \to N_A - G\kappa N_S$. Furthermore, we see that if $(1-1/G)\,(N_V+1) \ll N_B$, the performance of the conversion module does not change asymptotically. This is verified in Fig. 2.2 via calculating $r_{\text{C}\not\to\text{D}}^{(\text{LB})}/r_{\text{CS}}$ vs $\log_{10}\left[N_V\,(1-1/G)\right]$, where the factor of four (6 dB) advantage is seen at the $N_S \ll 1$ limit.

The same analysis can also be applied to the non-ideal scenario of imperfect heterodyne detection of the amplified mode and imperfect idler detection. Heterodyne detection efficiency in the microwave regime typically ranges from 40% to 70% depending on the input power. However, in the scope of our analysis, η_S represents the overall channel efficiency, which is dependent on the specific experiment and may be much lower, with realistic values around 10% or even less (down to 1%). Therefore, to account for the efficiencies of the detectors, we introduce two beamsplitters, as illustrated in Fig. 2.1, with transmissivities η_S and η_I, respectively. These beamsplitters combine the incoming modes a_A and a_I with their respective thermal modes a_{E_1} and a_{E_2}.

For simplicity, we assume the non-ideal heterodyne detection to be symmetric in the quadratures, resulting in the input-output relation

$$a_A' = \sqrt{\eta_S}a_A + \sqrt{1-\eta_S}a_{E_1}, \tag{2.13}$$

where we set $\left\langle a_{E_1}^{\dagger} a_{E_1} \right\rangle = N_{E_1}$. By performing the analysis through channel composition [see Eqs. (2.2), (2.10), and (2.13)], one can obtain

$$\begin{aligned} a'_A &= \mathrm{e}^{\mathrm{i}\theta} \sqrt{\eta_S G \kappa} a_S + \sqrt{1 - \eta_S G \kappa} \tilde{a}, \\ \tilde{a} &= \frac{\sqrt{\eta_S G (1-\kappa)} a_B + \sqrt{\eta_S (G-1)} a_V^{\dagger} + \sqrt{1-\eta_S} a_{E_1}}{\sqrt{1 - \eta_S G \kappa}}, \end{aligned} \tag{2.14}$$

with $\left[\tilde{a}, \tilde{a}^{\dagger}\right] = 1$, and

$$\left\langle \tilde{a}^{\dagger} \tilde{a} \right\rangle = \frac{\eta_S G N_B + \eta_S (G-1)(N_V + 1) + (1 - \eta_S) N_{E_1}}{1 - \eta_S G \kappa}. \tag{2.15}$$

With this composition, the channel is now characterised by the parameters

$$\begin{aligned} \kappa &\to \eta_S G \kappa, \\ N_B &\to \eta_S G \left[N_B + (1 - 1/G)(N_V + 1) + \frac{1 - \eta_S}{\eta_S G} N_{E_1} \right]. \end{aligned} \tag{2.16}$$

If we combine this reparameterization with an imperfect idler detection

$$a'_I = \sqrt{\eta_I} a_I + \sqrt{1 - \eta_I} a_{E_2}, \tag{2.17}$$

with $\left\langle a_{E_2}^{\dagger} a_{E_2} \right\rangle = N_{E_2}$, the CM of these two non-ideal modes a'_A and a'_I can be expressed as

$$\mathbf{V}'_{AI} = \begin{pmatrix} \left(2N'_A + 1\right)\mathbf{I} & V'_{12}\mathbf{RZ} \\ V'_{12}\mathbf{ZR}^T & \left(2N'_I + 1\right)\mathbf{I} \end{pmatrix}, \tag{2.18}$$

where we call

$$\begin{aligned} N'_A &= \eta_S G \left[\kappa N_S + N_B + (1 - 1/G)(N_V + 1) + \frac{1 - \eta_S}{\eta_S G} N_{E_1} \right], \\ V'_{12} &= 2\sqrt{\eta_S \eta_I G \kappa N_S (N_S + 1)}, \\ N'_I &= \eta_I \left(N_S + \frac{1 - \eta_I}{\eta_I} N_{E_2} \right). \end{aligned} \tag{2.19}$$

It is worth noting how the dominance of N'_A by N_B in Eq. (2.19) suggests that excess noise from the electronics may not play a significant role.

2.7 Correlation-to-displacement conversion in practice

Since the procedure has been extensively discussed in Ref. [131], we will not delve into it in this paper. By heterodyning mode a'_A, one obtains the remaining modes are still in a Gaussian state, resulting in the following expression for the output CM

$$\begin{aligned} \mathbf{V}'^{(Het)}_{I|A} &= (2E' + 1)\mathbf{I}, \\ E' &= N'_I - \frac{\eta_S \eta_I G \kappa N_S (N_S + 1)}{N'_A + 1}. \end{aligned} \tag{2.20}$$

Correspondingly, with measurement result $\overline{\mathbf{x}}_\Pi = (q_\Pi, p_\Pi)^T$, the mean of the non-ideal idler becomes

$$\overline{\mathbf{x}}'_I = \frac{\sqrt{\eta_S \eta_I G \kappa N_S \left(N_S + 1\right)}}{N'_A + 1} \begin{pmatrix} q_\Pi \cos\theta + p_\Pi \sin\theta \\ q_\Pi \sin\theta - p_\Pi \cos\theta \end{pmatrix}. \tag{2.21}$$

Here Π is just a subscript reminding ourselves that these are measurement outcomes. With the imperfections in consideration, the distribution of the measurement outcomes is given by

$$p\left(\overline{\mathbf{x}}_\Pi\right) = \frac{\exp\left(-\frac{\left|\overline{\mathbf{x}}_\Pi\right|^2}{4\left(N'_A+1\right)}\right)}{4\pi\left(N'_A + 1\right)}, \tag{2.22}$$

from which the distribution of $\mathcal{M}_m = \left(q_{\Pi_m} + \mathrm{i}p_{\Pi_m}\right)/2$ can be obtained as

$$p\left(\mathcal{M}_m\right) = \frac{\exp\left(-\frac{\left|\mathcal{M}_m\right|^2}{N'_A+1}\right)}{\pi\left(N'_A + 1\right)}. \tag{2.23}$$

Finally, by utilizing the displacement conditional on the heterodyne measurement result in the idler complex plane

$$d_m = \frac{\sqrt{\eta_S \eta_I G \kappa N_S \left(N_S + 1\right)}\mathrm{e}^{\mathrm{i}\theta}\mathcal{M}^\star_m}{N'_A + 1}, \tag{2.24}$$

we can express the total displacement of the collective idler mode at the output of the programmable beam splitter array, through a change of variables, as

$$\begin{aligned} \left|d_T\right|^2 &= \sum_{m=1}^{M} \left|d_m\right|^2 = \xi \sum_{i=1}^{2M} z_i^2, \quad z_i \sim \mathcal{N}\left(0,1\right), \\ \xi &= \frac{\eta_S \eta_I G \kappa N_S \left(N_S + 1\right)}{2\left(N'_A + 1\right)}, \end{aligned} \tag{2.25}$$

where $\mathcal{N}\left(0,1\right)$ denotes a Gaussian distribution with zero mean and unit variance. In the following sections, we will make extensive use of the parameter ξ, which plays a critical role in our analysis. We note that $\left|d_T\right|^2$ satisfies the χ^2 distribution Eq. (2.5), with mean $2M\xi$ and variance $4M\xi^2$. Furthermore, Eq. (2.20) can be conveniently rephrased as $E' = N'_I - 2\xi$.

2.7.1 Performance limits of the conversion module in practice

Here we introduce a further, commonly used, benchmark for analysing the illumination protocol, i.e., the Quantum Chernoff Bound (QCB). It provides an upper bound for the Helstrom error probability of Sec. 2.5, which is asymptotically tight in the error exponent for large M [144]. Thus, the error exponent of the QCB provides the best achievable error exponent, and must be larger than $r^{(\mathrm{LB})}_{\mathrm{C}\not\to\mathrm{D}}$.

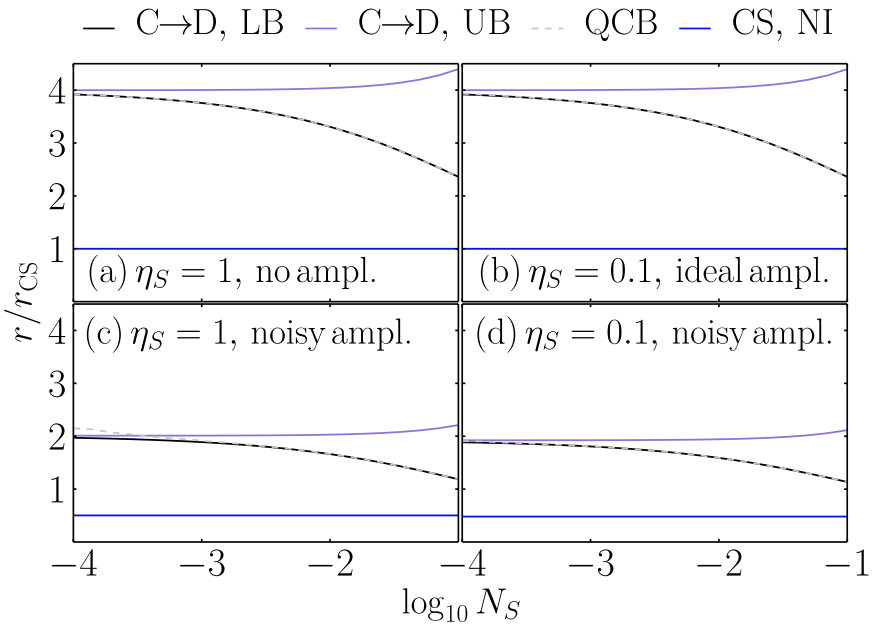

Figure 2.3: Black lines represent the ratio $r^{(\mathrm{LB})}_{\mathrm{C\to D}}/r_{\mathrm{CS}}$ as a function of $\log_{10} N_S$, purple ones $r^{(\mathrm{UB})}_{\mathrm{C\to D}}/r_{\mathrm{CS}}$, dashed gray for the QCB (see App. A.2), and blue ones $r^{(\mathrm{NI})}_{\mathrm{CS}}/r_{\mathrm{CS}}$, where $r^{\mathrm{NI}}_{\mathrm{CS}}$ is obtained by applying the substitution Eq. (2.16). (a) Ideal return detection, no additional signal loss $\eta_S = 1$ and therefore no amplification needed, $G = 1$. (b) Lossy return detection $\eta_S = 0.1$, assuming pure loss $N_{E_1} = 0$. We apply quantum-limited amplification of $G = 100$, $N_V = 0$. (c) Ideal return detection $\eta_S = 1$, and noisy amplification $G = 100$, $N_V = N_B$ at room temperature. (d) Lossy return detection $\eta_S = 0.1$ with noise $N_{E_1} = N_B$ at room temperature. We apply noisy amplification $G = 100$, $N_V = N_B$ at room temperature. The lower bound of the C→D module consistently aligns with the QCB.

The comparison between the error exponent of the C→D module [see Eq. (2.8) and that for the upper bound, which is within the text] and the one obtained from the QCB (see App. A.2 for further details) can be seen in Fig. 2.3, showing that even in the worst case scenario of lossy amplification and imperfect detection, there is a factor of 2 improvement compared to the classical case Eq. (2.9). Furthermore, it is worth noting that the lower bound of the conversion module consistently exhibits a close alignment with the QCB. The plots in Fig. 2.4 provide evidence for the importance of an amplification stage in the microwave domain, where losses from detection may be challenging to overcome. It compares the ratio $r^{(\mathrm{LB})}_{\mathrm{C\to D}}/r_{\mathrm{CS}}$ with $r^{(\mathrm{NI})}_{\mathrm{CS}}/r_{\mathrm{CS}}$ versus $\log_{10} G$, in two different temperature conditions (cool and warm). It can be seen that amplification is not necessary in a cool environment, but it is crucial in practical cases characterized by warm environments where $\eta_S < 1/2$: only through amplification can a factor of 2 advantage be achieved, with the emergence of an optimal value of G. In the later part of the paper, we will refer to the parameter setting above as either the “cool case” or the “warm case”, referring to the

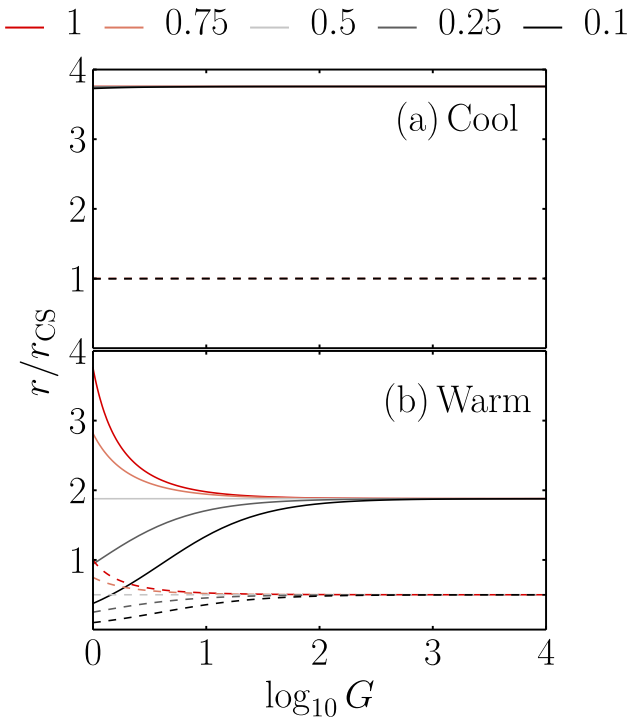

Figure 2.4: The impact of losses and gain on two scenarios: (a) a cool case with $N_V = N_{E_1} = 0.1$ (corresponding to $T_S = 100$ mK) and (b) a warm one with $N_V = N_{E_1} = N_B$ (corresponding to $T_S = 300$ K). The other parameters are fixed at $N_B = 1250$, $\kappa = 0.01$, $N_S = 10^{-3}$, and $\eta_I = 1$ (i.e., we assume the idler is ideally stored). Solid lines represent the ratio $r^{(\mathrm{LB})}_{\mathrm{C\not\to D}}/r_{\mathrm{CS}}$ as a function of the gain $\log_{10} G$, for different values of η_S (visible in the legend); dashed lines $r^{(\mathrm{NI})}_{\mathrm{CS}}/r_{\mathrm{CS}}$, where $r^{\mathrm{NI}}_{\mathrm{CS}}$ is obtained by applying the substitution Eq. (2.16). Amplification is not necessary in a cool environment (a), but it is crucial in practical cases characterized by warm environments (b) where $\eta_S < 1/2$: only through amplification can a factor of 2 advantage be achieved.

processing temperature of the returned signal.

2.7.2 Kennedy receiver

Let us now study the performance of the C↛D module in the case of a specific detection scheme of the conditional idler state. A simple idler's detection scheme is the classical Kennedy receiver, described by the set of POVMs $\Pi_0 = |0\rangle\langle 0|$ and $\Pi_1 = \mathbb{1} - \Pi_0$, where $\mathbb{1}$ is the identity operator and $|0\rangle\langle 0|$ represents the absence of a photon. The receiver operates in the on/off mode and distinguishes between the presence or absence of a photon.

A practical approach to implement such a receiver is described in Ref. [118], where the authors introduce a method based on a photo-current and photo-counting discriminator. While the calibration and measurement of every parameter in their

system are rather complex, the basic idea is to use a dispersive qubit to read out single photons in a regime where the probability of having more than one photon is low.

We present a simple approach that provides useful insights and motivates the adoption of a Kennedy receiver, but we will not employ it for our analysis. In the limit where the number of signal photons $N_S \ll 1$ is low, the receiver (neglecting experimental limitations) accurately selects $|0\rangle$ as the measurement outcome. However, the uncertainty in the decision arises from the fluctuations in the coherent state $|\alpha\rangle$. When the least probable classical situation $p_0 = p_1 = 1/2$ is considered, the error probability can be calculated as [131]

$$p_e = \frac{1}{2}\langle\alpha|\,\Pi_1\,|\alpha\rangle = \frac{1}{2}\mathrm{e}^{-|\alpha|^2} \sim 2P_{\mathrm{H}} \Rightarrow P_K \sim 2P_{\mathrm{C\to D}}, \tag{2.26}$$

when $|\alpha| \gg 1$ [see Eq. (2.6)] .

Nevertheless, the idler photon counting formula Eq. (2.26) only considers the ideal case of vacuum versus coherent state. To account for deviations from this ideal scenario, we introduce a Kennedy receiver that attempts to discriminate between two differently displaced thermal states at finite N_S. In the P-representation, the two density operators to be distinguished are described by [145]

$$\rho_{th}(\delta) = \int_{\mathbb{C}} \frac{d^2\beta}{\pi N_T}\,\exp\left[-\frac{|\beta-\delta|^2}{N_T}\right]|\beta\rangle\langle\beta|\,, \tag{2.27}$$

where $\delta = \left\{0,\ \sqrt{x}\right\}$ is the phase-space displacement, and $N_T = N_I' - \{0,\, 2\xi\}$ represents the average number of photons produced by thermal noise, with N_I' and ξ defined in Eqs. (2.19) and (2.25), respectively. The error probability can then be calculated using the two POVMs as

$$\begin{aligned} p_e &= p_0\mathrm{Tr}\left[\Pi_1\rho_{th}(0)\right] + p_1\mathrm{Tr}\left[\Pi_0\rho_{th}(\alpha)\right] \\ &= p_0\left\{\mathbb{1} - \mathrm{Tr}\left[\Pi_0\rho_{th}(0)\right]\right\} + p_1\mathrm{Tr}\left[\Pi_0\rho_{th}(\alpha)\right], \end{aligned} \tag{2.28}$$

where $\mathrm{Tr}\left[\Pi_0\rho_{th}(\delta)\right] = \exp\left(-\frac{|\delta|^2}{N_T+1}\right)/(N_T+1)$ [see Eq. (E1) of Ref. [136]]. Applied to our case, the least classical probability situation $p_0 = p_1 = 1/2$ yields

$$p_e = \frac{1}{2}\left[1 + \frac{\exp\left(-\frac{x}{N_I'+1-2\xi}\right)}{N_I'+1-2\xi} - \frac{1}{N_I'+1}\right]. \tag{2.29}$$

Finally, the error probability of the Kennedy receiver is given by

$$P_K = \int_0^{+\infty} dx\, P^{(M)}(x;\,\xi)\, p_e, \tag{2.30}$$

with $P^{(M)}(x;\,\xi)$ given in Eq. (2.5). In other words

$$P_K = \frac{1}{2\left(N_I'+1\right)}\left[\left(1 + \frac{2\xi}{N_I'+1-2\xi}\right)^{1-M} + N_I'\right]. \tag{2.31}$$

While we have adopted the Kennedy receiver in this work, it is worth noting that further performance improvements can be achieved by optimizing the displacement amplitude and consider the improved Kennedy receiver [146].

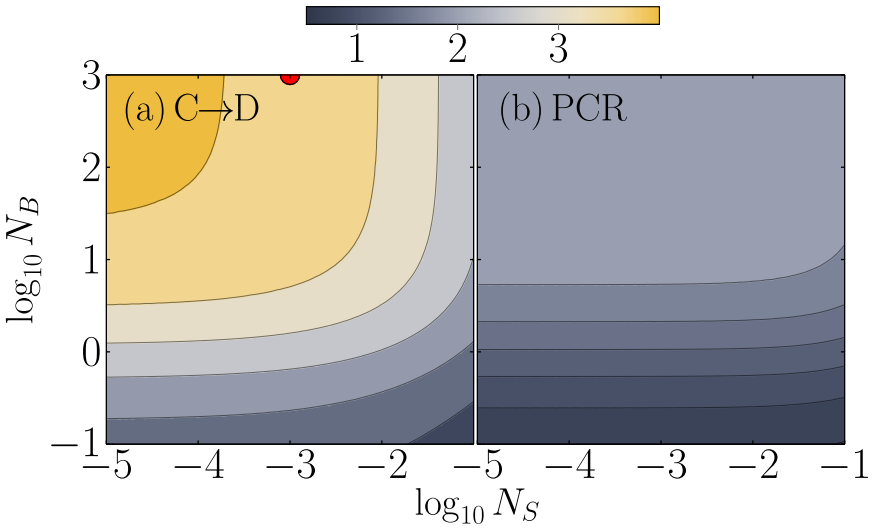

Figure 2.5: Comparison of the error exponent ratio r/r_{CS} between the C↛D module and the PCR [see Eqs. (2.8), (2.33), and (2.9), respectively] as a function of $\log_{10} N_S$ and $\log_{10} N_B$. The other parameters correspond to the 'cool' case and are set to: $N_V = N_{E_1} = N_{V_{\mathrm{PCR}}} = 0.1$ (corresponding to $T_S = 100$ mK), $N_{E_2} = 4 \times 10^{-11}$ (corresponding to $T_I = 10$ mK), $G = 100$, $G_{\mathrm{PCR}} = 2$, $\eta_S = 0.1$, and $\eta_I = 0.9$. The red circle represents the parameters used in Fig. 2.6. The C↛D module possesses clear better performance, as stated by the wide yellowish areas.

2.8 Performance benchmarks

In order to assess the performance of the C↛D module, we compare it with a classical benchmark based on coherent states and homodyne detection. The error probability of homodyne detection is given by [107]

$$P_{\mathrm{E,\,homo}} = \frac{1}{2}\,\mathrm{erfc}\left[\sqrt{\frac{\kappa M N_S}{2\,(2N_B+1)}}\right], \tag{2.32}$$

where $\mathrm{erfc}[z] = \left(2/\sqrt{\pi}\right)\int_z^{+\infty} dt\, e^{-t^2}$ is the complementary error function. Besides the classical scheme, we also benchmark with known practical receivers for QI such as the PCR scheme [129], [131], whose error probability in the QI scenario is simply given by (details can be found in App. A.3)

$$\begin{aligned} P_{\mathrm{E,PCR}} &= \frac{1}{2}\,\mathrm{erfc}\left(\sqrt{R_{\mathrm{PCR}} M}\right), \\ R_{\mathrm{PCR}} &= \frac{\mu_1^2}{4}\Big[2N_I' + (G_{\mathrm{PCR}}-1)\left(2N_I'+1\right)\left(N_A' + N_{A,\,\kappa=0}' + 2\right) \\ &\quad + \mu_1^2/2 + 2G_{\mathrm{PCR}} N_{V_{\mathrm{PCR}}}\Big]^{-1}, \end{aligned} \tag{2.33}$$

where μ_1 is given by Eqs. (A.17), and G_{PCR} and $N_{V_{\mathrm{PCR}}}$ correspond to the gain and mean number of added photons of the phase conjugator, respectively. Fig. 2.5 shows

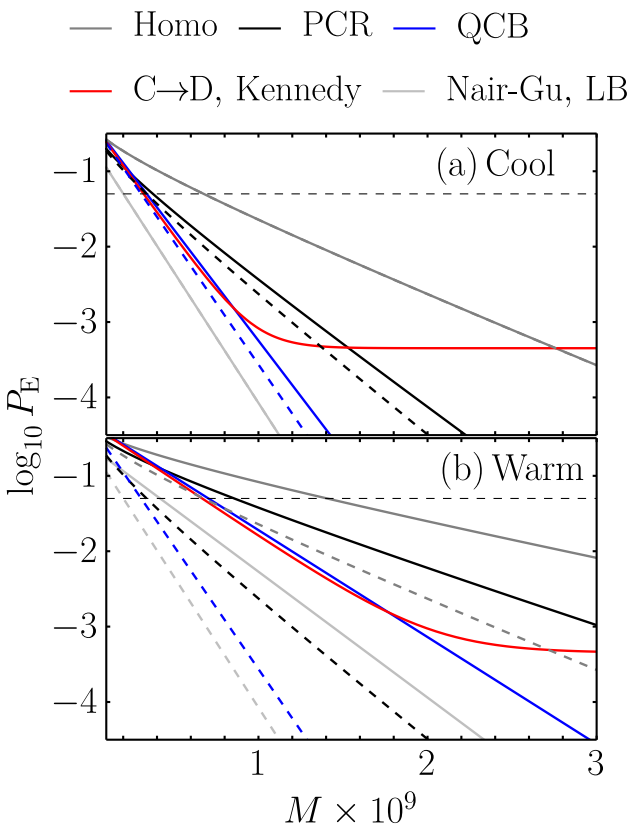

Figure 2.6: Error probability as a function of the number of copies M in both the non-ideal (solid) and ideal (dashed) case. The non-ideal case is characterised by: $N_S = 10^{-3}$, $N_B = 1250$, $N_{E_2} = 4 \times 10^{-11}$ (corresponding to $T_I = 10$ mK), $\kappa = 0.01$, $G = 100$, $\eta_S = 0.1$, $\eta_I = 0.9$, and $G_{\mathrm{PCR}} = 2$. (a) Cool case with $N_V = N_{E_1} = N_{V_{\mathrm{PCR}}} = 10^{-1}$ (corresponding to $T_S = 100$ mK), (b) warm one $N_V = N_{E_1} = N_{V_{\mathrm{PCR}}} = 1250$ (corresponding to $T_S = 300$ K). Dashed lines are the performance for each solid colored curve in the ideal scenario ($\eta_S = \eta_I = 1$ and no amplification $G = 1$). The horizontal dashed line marks $P_{\mathrm{E,\,homo}} = 0.05$.

a comparison between the performance limits of the C→D module and PCR in terms of error exponents [see Eqs. (2.8) and (2.33), respectively]. Although we only present the performance analysis for the cool case of return signal processing, it is noteworthy that the C→D module exhibits superior performance compared to the PCR, as evidenced by a significantly larger region of parameter space with better performance, as indicated by the yellow coloration. The scaling of major error probabilities with the number of copies M is shown in Fig. 2.6, for both the warm and cool cases. Note that the parameter setting of Fig. 2.6 corresponds to the red dot in Fig. 2.5. Specifically, we focus on the performance of the C→D module with Kennedy receiver (red lines), which is almost comparable to that of the QCB (blue) and outperforms any other practical scheme considered. The saturation of the C→D performance is due to the on-off detection of Kennedy receiver, as we will resolve

in Sec. 2.9. We also present the comparison to the Nair-Gu lower bound [132] (light gray), which shows similar scaling of the QCB. In Fig. 2.5, the dashed curves are the performance curves of the receivers assuming all equipment become ideal, instead the solid curves where imperfections are considered (the same color coding of the curves are adopted for both dashed and solid, as indicated by the legend). To provide a comparison between the C↛D module equipped with an on/off Kennedy receiver and the PCR, Fig. 2.7 presents the error probability ratio $\log_{10}(P_E/P_{\mathrm{E,homo}})$ for the cool case, where M is chosen such that the homodyne error probability is fixed at $P_{\mathrm{E,homo}} = 0.05$. As shown by the wide dark area, the C↛D module clearly outperforms the PCR in the $N_B \gg 1$, $N_S \ll 1$ parameter regime.

2.9 Enhanced performance with number-resolving detection

So far we have adopted the Kennedy receiver with on-off detection, which leads to the saturation of error probability (red lines) in Fig. 2.6 at large M. To obtain better performance, in this section we generalize the Kennedy receiver to a photon number resolving detector (PNRD) on the idler.

As already analyzed, the decision between the presence or absence of the target is equivalent to discriminating between two states of the final idler mode after the beamsplitter array: the thermal state $\rho_{0,N_I'}$ when the target is absent, and the displaced thermal state $\rho_{\sqrt{x},E'}$ when it is present. Recall that N_I' is defined by Eq. (2.19), E' by Eq. (2.20), and x is a random variable associated with the results of M heterodyne measurements on the return modes, distributed according to Eq. (2.5), with ξ given by Eq. (2.25). With a PNRD detection, we can now compare the photon number probability distributions for the two hypotheses: $p_n^{(0)} = \langle n|\rho_{0,N_I'}|n\rangle$ and $p_n^{(1)}(x) = \langle n|\rho_{\sqrt{x},E'}|n\rangle$. The presence of the target is declared when the outcome of the photon number measurement is greater than a predetermined threshold value, $n \geq n_D \geq 1$.

To prepare our analyses for the ROC curve, we consider the false alarm probability P_F and the detection probability P_D for a fixed decision threshold n_D as

$$P_F = \sum_{n=n_D}^{+\infty} \langle n|\rho_{0,N_I'}|n\rangle, \tag{2.34}$$

$$P_D = \sum_{n=n_D}^{+\infty} \int_0^{+\infty} dx\, P^{(M)}(x;\xi)\, \langle n|\rho_{\sqrt{x},E'}|n\rangle, \tag{2.35}$$

where we average over the random variable x. The evaluation of P_F is simple and one has

$$P_F(n_D) = \left(\frac{N_I'}{N_I'+1}\right)^{n_D}, \tag{2.36}$$

while that of P_D is more involved. We start by using the following result for the

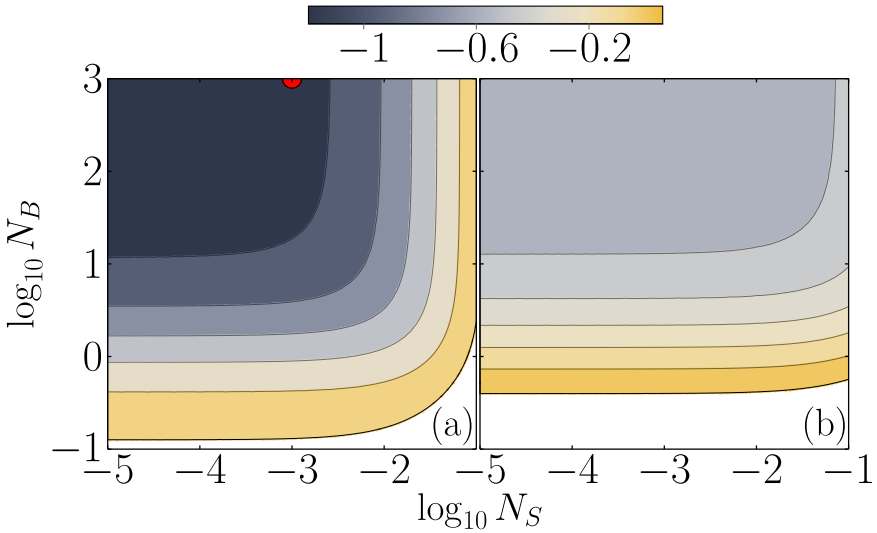

Figure 2.7: Comparison based on the error probability ratio $\log_{10}(P_E/P_{\mathrm{E,homo}})$ between (a) the C↛D module (equipped with an on/off Kennedy receiver) and (b) the PCR [see Eqs. (2.31), (2.33), and (2.32), respectively] vs. $\log_{10} N_S$ and $\log_{10} N_B$. The value of M is selected to set $P_{\mathrm{E,homo}} = 0.05$. The other parameters correspond to the 'cool' case and are: $N_V = N_{E_1} = N_{V_{\mathrm{PCR}}} = 0.1$, $N_{E_2} = 4 \times 10^{-11}$, $G = 100$, $G_{\mathrm{PCR}} = 2$, $\eta_S = 0.1$, and $\eta_I = 0.9$. The red circle indicates the parameters used in Fig. 2.6. As shown by the wide dark area, the C↛D module outperforms the PCR.

photon statistics of a displaced thermal state for a given x [147], [148]

$$p_n^{(1)}(x) = \frac{\exp\left(-\frac{x}{E'+1}\right)}{E'+1}\left(\frac{E'}{E'+1}\right)^n L_n\left[-\frac{x}{E'(E'+1)}\right], \tag{2.37}$$

where $L_n[\cdot]$ is the n-th Laguerre polynomial. Next, one can perform the average over the probability distribution Eq. (2.5) to obtain the average photon number probability distribution when the target is present

$$\begin{aligned}\bar{p}_n^{(1)}(M;\xi) = {} & \frac{(E'+1)^{M-n-1}E'^n}{(E'+1+2\xi)^M} \\ & \times {}_2F_1\left[M,\,-n,\,1,\,-\frac{2\xi}{E'(E'+1+2\xi)}\right],\end{aligned} \tag{2.38}$$

where ${}_2F_1(a, b, c, z)$ is the Gaussian hypergeometric function. Consequently, the detection probability $P_D(n_D)$ can be exactly determined as

$$P_D(n_D) = 1 - \sum_{n=0}^{n_D-1} \bar{p}_n^{(1)}(M;\xi). \tag{2.39}$$

2.9.1 Bayesian error probability

To begin with, we consider the symmetric error $P_E = (P_F + 1 - P_D)/2$ and evaluate the performance. Here the results are similar to that of Ref. [140]. This is

because, given the choice of photon counting, random phase does not change the performance anymore. From Eqs. (2.38) and (2.36), we have the error probability P_E as a function of the threshold n_D. We compare this optimal decision strategy with a variable threshold n_D, and quantify the error of probability using

$$P_{\mathrm{C}\not\to\mathrm{D}}^{(n_D)} = \frac{1}{2}\left[1 - \sum_{n=0}^{n_D-1} \gamma_n\left(2M;\, \xi\right)\right], \tag{2.40}$$

where the function

$$\begin{aligned}\gamma_n\left(M;\, \xi\right) = &\frac{N_I'^n}{\left(N_I'+1\right)^{n+1}} \\ &- \frac{(E'+1)^{M-n-1}E'^n}{(E'+1+2\xi)^M}\,{}_2F_1\left[M,\, -n,\, 1,\, -\frac{2\xi}{E'(E'+1+2\xi)}\right].\end{aligned} \tag{2.41}$$

Although the above equation is exact, to enable efficient numerical evaluation in all parameter region of interest, we further make an approximation at the $M \gg 1$ limit and obtain

$$\begin{aligned}\gamma_n\left(M;\, \xi\right) \simeq &\frac{N_I'^n}{\left(N_I'+1\right)^{n+1}} \\ &- \frac{E'^n}{(E'+1)^{n+1}}\mathrm{e}^{-2M\xi/E'}\,{}_1F_1\left[n+1,\, 1,\, \frac{2M\xi}{E'\left(E'+1\right)}\right].\end{aligned} \tag{2.42}$$

The precision of such an approximation is sufficient for our evaluation, as verified in Ref. [140]. The optimal performance is then given by a minimization of the error probability over the threshold n_D

$$P_{\mathrm{C}\not\to\mathrm{D}}^{(opt)} = \min_{n_D \geq 1} P_{\mathrm{C}\not\to\mathrm{D}}^{(n_D)}. \tag{2.43}$$

Note that $P_{\mathrm{C}\not\to\mathrm{D}}^{(1)} \equiv P_K$ [see Eq. (2.31)], as expected.

Fig. 2.8 shows the results of our analysis, using the same parameter values as in Fig. 2.6. We observe that the optimized approach (orange) produces results that are comparable to those of the non-ideal QCB (blue, see also App. A.2). Specifically, the irregular trend in the data is well described by a variable threshold decision strategy approach, which is represented by the dashed lines in the figure. Our findings suggest that the optimized approach can effectively discriminate between the two states of interest, even in the presence of noise and other imperfections.

2.9.2 Receiver operating characteristic

Conversion module and photon-number resolving detector

Let us now analyse the performance of the C↛D module within the Neyman-Pearson framework, which is suitable in some radar operations [149], using ROC curves. In this approach, a chosen false alarm probability P_F is fixed, and the goal is to

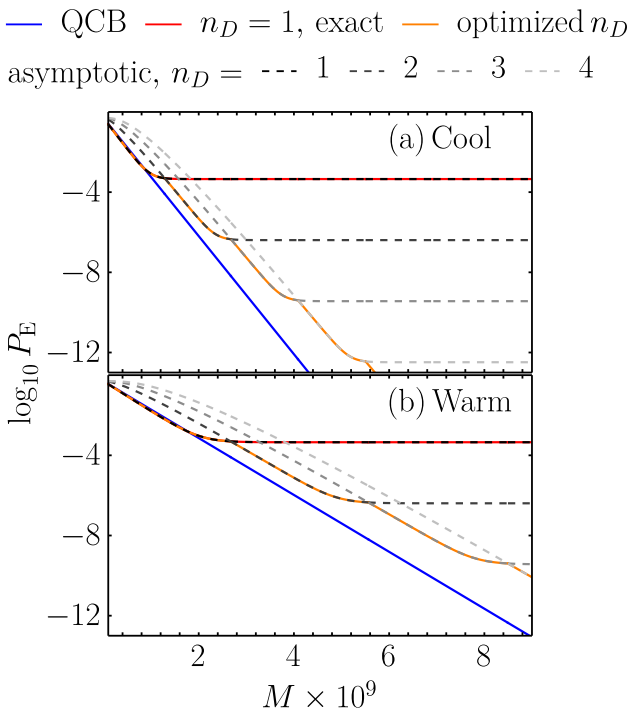

Figure 2.8: The saturation of the red line in Fig. 2.6 suggests an improvement, following the lines of Ref. [140], where a variable threshold decision strategy approach has been used for asymptotic analysis. The red curve reproduces the usual Kennedy receiver corresponding to the fixed threshold $n_D = 1$. The dashed grey lines corresponds to the case of fixed, increasing values of n_D. The orange line gives the optimized result in which n_D is adjusted according to M, and therefore to the two states to be discriminated. This latter approach yields results comparable to those of the non-ideal QCB (blue). Parameter values are the same as those of Fig. 2.6.

maximize the detection probability P_D. By gradually reducing the threshold value n_D from a high (ideally infinite) value to zero, a concave ROC curve can be obtained, plotting P_D versus P_F, starting from $P_F = P_D = 0$ and ending at $P_F = P_D = 1$.

To gain a clearer understanding of the behavior of the ROC curve, we derive an analytical expression based on a Gaussian approximation. When $x \gg 1$, the probability distribution $p_n^{(1)}(x)$ Eq. (2.37) can be represented by a Gaussian distribution with mean $\langle n(x)\rangle = E' + x$, and variance $\sigma_n^2(x) = \left\langle n^2(x)\right\rangle - \langle n(x)\rangle^2 = E'^2 + E' + x(2E' + 1)$. As a result, in this limit, the average probability distribution Eq. (2.38) can also be approximated by a Gaussian distribution with properly averaged mean and variance, and we have

$$\bar{p}_n^{(1)}(M;\xi) \sim \frac{1}{\sqrt{2\pi\sigma_n^2}} \exp\left[-\frac{(n-\bar{n})^2}{2\sigma_n^2}\right], \tag{2.44}$$

with

$$\begin{aligned} \bar{n} &= E' + \bar{x} \\ &= E' + 2M\xi, \end{aligned} \tag{2.45}$$

$$\begin{aligned} \sigma_n^2 &= E'^2 + E' + \bar{x}\,(2E' + 1) + \sigma_x^2 \\ &= E'^2 + E' + 2M\xi\,(2\xi + 2E' + 1)\,, \end{aligned} \tag{2.46}$$

taking into account that the distribution Eq. (2.5) has mean $\bar{x} = 2M\xi$, and variance $\sigma_x^2 = 4M\xi^2$. A necessary condition for the validity of such a Gaussian treatment is that $\bar{x} = 2M\xi \gg 1$. By using the Gaussian approximation Eq. (2.44), and eliminating the threshold n_D with the aid of Eq. (2.36), one gets the following approximate expression for the ROC curve of the C↛D module

$$P_D\,(P_F) \sim \frac{1}{2}\,\mathrm{erfc}\left[\frac{1}{\sigma_n\sqrt{2}}\left(\frac{\log P_F}{\log\left(\frac{N_I'}{N_I'+1}\right)} - \bar{n}\right)\right]. \tag{2.47}$$

This approximation provides a satisfactory description of the ROC curves for moderate values of P_D and P_F as long as $2M\xi > 1$. Although the average probability distribution $\bar{p}_n^{(1)}\,(M;\,\xi)$ resembles a Gaussian distribution around the peak centered at its average value, it decays exponentially, not Gaussianly, for $P_F \to 0 \Rightarrow P_D \to 0$, i.e., $n_D \to \infty$. As a result, Eq. (2.47) tends to underestimate the value of P_D for high threshold values n_D.

The ROC curve in the case of the PCR

As discussed in App. A.3 (see also Ref. [150]), when $M \gg 1$, the photo-count difference of the PCR, $N = N_+ - N_-$, according to the central limit theorem, follows a Gaussian distribution with a probability density for the two hypotheses

$$P_{N|H_{0/1}}\,(n|H_{0/1}) = \frac{\exp\left[-\frac{(n-M\mu_{0/1})^2}{2M\sigma_{0/1}^2}\right]}{\sqrt{2\pi M\sigma_{0/1}^2}}, \tag{2.48}$$

where the two mean values $\mu_{0/1}$ and the two variances $\sigma_{0/1}^2$ are given by Eqs. (A.17).

The discrimination between two Gaussian distributions with different means and variances can be obtained by using the extended van Trees approximation [151], and it can be expressed in terms of the auxiliary function

$$\begin{aligned} \mu(s) = \ln\Bigg\{ & \frac{\sigma_1^{1-s}\sigma_0^s}{\sqrt{s\sigma_0^2 + (1-s)\,\sigma_1^2}} \\ & \times \exp\left\{-\frac{M\,(\mu_0-\mu_1)^2\,s\,(1-s)}{2\left[s\sigma_0^2 + (1-s)\,\sigma_1^2\right]}\right\}\Bigg\}, \end{aligned} \tag{2.49}$$

where s is a threshold parameter. The false alarm and detection probabilities are then respectively given by

$$\begin{aligned} P_F &= \frac{1}{2}\mathrm{erfc}\left[s\sqrt{\frac{\ddot{\mu}(s)}{2}}\right], \\ P_D &= 1-\frac{1}{2}\mathrm{erfc}\left[(1-s)\sqrt{\frac{\ddot{\mu}(s)}{2}}\right], \end{aligned} \tag{2.50}$$

where $\ddot{\mu}(s) \equiv d^2\mu/ds^2$.

However, one can get a simpler and clearer expression by taking into consideration that the variances for the two hypothesis, σ_0^2 and σ_1^2, are nearly identical for the typical parameter values in a microwave QI experiment, that is, when $\kappa \ll 1$, $N_S \ll 1$, and $N_B \gg 1$. In fact, Eqs. (A.17) give

$$\begin{aligned} &\frac{\sigma_1^2-\sigma_0^2}{\sigma_0^2} = \eta_S G\left(G_{\mathrm{PCR}}-1\right)\kappa N_S\left[2N_I'+1+2\eta_I\left(N_S+1\right)\right] \\ &\times\left[N_I'+\left(G_{\mathrm{PCR}}-1\right)\left(2N_I'+1\right)\left(N_{A,\,\kappa=0}'+1\right)+G_{\mathrm{PCR}}N_{V_{\mathrm{PCR}}}\right]^{-1}, \end{aligned} \tag{2.51}$$

which scales as $\kappa N_S/N_B \ll 1$ when $N_B \gg N_S$. As a result, one has $\ddot{\mu}(s) = M\mu_1^2/\sigma_1^2 \equiv d_{\mathrm{PCR}}^2$ in Eqs. (2.50), which can be rewritten as

$$\begin{aligned} P_F &= \frac{1}{2}\mathrm{erfc}\left[\frac{1}{\sqrt{2}}\left(\frac{\ln\eta}{d_{\mathrm{PCR}}}+\frac{d_{\mathrm{PCR}}}{2}\right)\right], \\ P_D &= \frac{1}{2}\mathrm{erfc}\left[\frac{1}{\sqrt{2}}\left(\frac{\ln\eta}{d_{PCR}}-\frac{d_{\mathrm{PCR}}}{2}\right)\right], \end{aligned} \tag{2.52}$$

where we introduce the new threshold parametrization as $\ln\eta = (s-1/2)\,d_{\mathrm{PCR}}^2$. By eliminating this threshold parameter, the analytical expression of the ROC curve for the PCR can be obtained as

$$P_D = \frac{1}{2}\mathrm{erfc}\left[\mathrm{erfc}^{-1}\left(2P_F\right)-\frac{d_{\mathrm{PCR}}}{\sqrt{2}}\right], \tag{2.53}$$

where $\mathrm{erfc}^{-1}(z)$ is the inverse of the complementary error function. We notice that the ROC curve for the PCR is analytically identical to that of the optimal classical benchmark of using coherent states and homodyne detection. Both have the same form as in Eq. (2.53), but the replacement $d_{\mathrm{PCR}} \to d_{\mathrm{CS}} = 2\sqrt{M\kappa N_S/\left(2N_B+1\right)}$ [150].

Fig. 2.9 presents the behavior of the ROC curve for the C→D module in both warm and cool cases, considering losses and amplification in the detection scheme. The results are compared to the corresponding Gaussian approximation Eq. (2.47), the PCR Eq. (2.53), and the non-ideal classical benchmark [using Eq. (2.53) with $d_{\mathrm{PCR}} \to d_{\mathrm{CS}}$ and Eq. (2.16)], all obtained under the same experimental conditions.

When the Neyman-Pearson decision strategy is considered, it can be observed that the C→D module exhibits excellent performance in both the cool and warm cases. In particular, its ROC curve is significantly larger than those obtained with the PCR and the classical approach for the same experimental conditions.

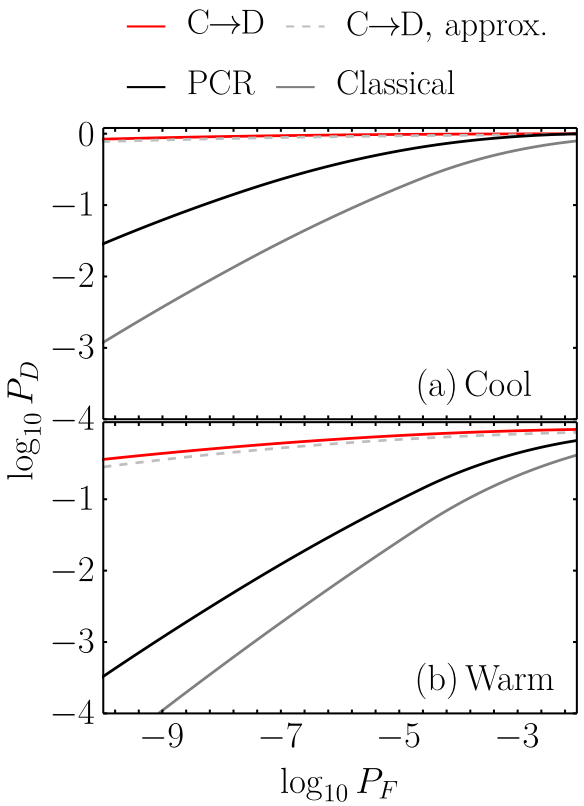

Figure 2.9: Comparison of ROC curves. The red line shows the performance of the C↛D module with a PNRD; the black one that of the PCR given by Eq. (2.53); the dashed light gray line depicts the performance of the Gaussian approximation of Eq. (2.47); the full dark grey line gives the non-ideal classical benchmark [using Eq. (2.53) with $d_{\mathrm{PCR}} \to d_{\mathrm{CS}}$ plus Eq. (2.16)]. The parameters used are the same as in Fig. 2.5 and 2.7 (indicated by the red dots there), with $M = 69 \times 10^7$.

2.10 Conclusions

In conclusion, this work analyzed how experimental imperfections can be mitigated using correlation-to-displacement conversion-based receivers, and our results showed that amplification on the return signals can effectively compensate for additional loss in the heterodyne detection. We also employed a Kennedy receiver for idler detection conditioned on heterodyne and demonstrated that in the ideal case, such a scheme has the optimal error exponent. In practical scenarios, such a receiver still provides quantum advantages over classical optimal schemes and outperforms other known practical receivers for quantum illumination.

Compared to sub-optimal receivers like OPA and PCR, the receiver design proposed in Ref. [131] and further developed here, based on C↛D conversion, not only achieves optimality but also eliminates the need for direct interaction between the idlers and the returns. This is particularly advantageous for microwave quantum illumination, where idlers require low-temperature cooling and isolation, while the

returns are noisy and at room temperature. By relying only on heterodyne and photon detection, this receiver design significantly reduces the technical challenges associated with optimal receivers, as compared to previous proposals based on sum-frequency generation [130].

Recent attention has focused on exploring non-Gaussian states as quantum probes in QI [152], [153]. However, it is established that TMSV states are asymptotic optimal for QI with a given signal photon number [132], [137], [154]: Ref. [137] proved the optimality for asymmetric hypothesis testing, while Refs. [132], [154] find TMSV to be optimal in the symmetric hypothesis testing in the weak reflectivity and large noise limit. The C→D conversion scheme described in this study could also be extended to the non-Gaussian scenario. Although the analysis may be more complex, our findings indicate that comparable asymptotic performance can potentially be achieved.

Overall, our findings illustrate the feasibility of practical microwave quantum illumination systems that can overcome experimental imperfections and offer quantum advantages for target detection in noisy environments. These insights can inform the development of future quantum illumination systems and contribute to the advancement of quantum sensing technologies.

Chapter 3

Conclusions

With this doctoral thesis, we have delved into two compelling research endeavors, each constituting a dedicated chapter. The inaugural chapter outlines our efforts in steering a quantum array towards a pure, steady state composed of many entangled qubit pairs. The key to this achievement lies in our adept manipulation of dissipative dynamics within a singular central element, whether it be a cavity or a qubit. We have verified that the purity of the resulting state endures when dissipation exclusively engages the central element. Intriguingly, even in the presence of supplementary decoherence affecting other qubits, the stationary state transforms into an entangled mixed state, resiliently retaining substantial entanglement. This robustness particularly manifests when the decay rate of supplementary dephasing processes follows behind that of the dissipative decay rate of the central element.

The versatility of our models finds resonance in their broad applicability across diverse physical scenarios, spanning atomic systems and solid-state nano-devices. This adaptability facilitates the realization of both chain and star geometries, thereby promoting practical applications in quantum information processing. Our work suggests an interesting path for future research, exploring whether similar methods can be used to create more complex entangled qubit states, such as the graph states crucial for measurement-based quantum computers.

Shifting the focus to our second chapter, we undertook a comprehensive analysis of how experimental imperfections can be effectively mitigated within the context of quantum illumination. Our exploration hinged upon correlation-to-displacement conversion-based receivers, showing how amplification on return signals skillfully compensates for additional loss in heterodyne detection. The introduction of a Kennedy receiver for idler detection conditioned on heterodyne revealed its optimality under ideal conditions and quantum advantages over classical optimal schemes in practical scenarios. Our proposed receiver design, rooted in C$\to$D conversion, not only attains optimality but also eliminates the need for direct interaction between idlers and returns — a distinct advantage, especially in the context of microwave quantum illumination.

In contrast to sub-optimal receivers like OPA and PCR, our design outperforms known practical receivers, particularly in the case of microwave systems. By relying solely on heterodyne and photon detection, our receiver design notably reduces the

technical challenges associated with optimal receivers, setting it apart from previous proposals based on sum-frequency generation.

Our findings also hint at the potential extension of the C↛D conversion scheme to the non-Gaussian scenario. While the analysis may introduce additional complexity, our results suggest that comparable asymptotic performance is within reach.

This thesis unfolds profound insights into the realm of quantum technologies, uncovering the intricacies of controlling quantum arrays and adeptly navigating experimental imperfections in quantum illumination systems. As a result, it guides future developments in quantum information processing, sensing technologies, and the practical realization of quantum illumination systems.

Appendices

Appendix A

About Chapter 2

A.1 Correlation-to-displacement converter

This section provides insight into the functionality of the conversion module, as discussed in Ref. [131]. Fundamentally, the module utilizes signal-idler correlations to facilitate conditional measurements and feed-forward processes. Specifically, the mth return mode undergoes heterodyning with the measurement result $\mathcal{M}$. Following this measurement, the mth idler conditional state assumes a displaced thermal state characterized by $E \sim N_S$ noise photons and displacement

$$d_m \sim \langle a_R a_I \rangle \frac{\mathcal{M}_m}{N_B} \sim \sqrt{\frac{\kappa N_S}{N_B}}. \tag{A.1}$$

Specifically, the outcomes of measurements govern the transmissions of a programmable beamsplitter array, sketched in Fig. A.1. The array comprises $M-1$ beamsplitters, $M-1$ undisplaced thermal output idler modes, and a single relevant output idler mode subject to collective displacement

$$|d_T| = \sqrt{\sum_{m=1}^{M} |d_m|^2}, \tag{A.2}$$

with $|d_T|^2$ satisfying the χ^2 distribution Eq. (2.5)

$$P^{(M)}(x;\, \xi) = \frac{x^{M-1} \mathrm{e}^{-x/(2\xi)}}{(2\xi)^M \Gamma(M)}, \quad \xi = \frac{\kappa N_S (N_S + 1)}{2(\kappa N_S + N_B + 1)}. \tag{A.3}$$

This implies that the average error probability can be expressed as Eq. (2.6), namely

$$P_{\mathrm{C}\to\mathrm{D}} = \int_0^{+\infty} dx\, P^{(M)}(x;\, \xi)\, P_{\mathrm{H}}\left(\rho_{0,N_S}, \rho_{\sqrt{x},E}\right). \tag{A.4}$$

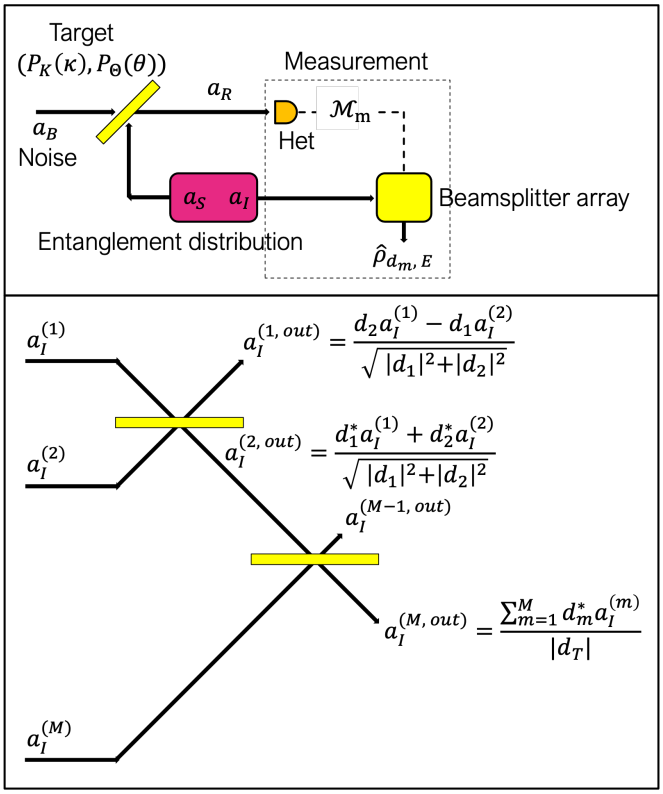

Figure A.1: (a) Schematic representation of the conversion module. (b) Programmable beamsplitter array with $M-1$ beamsplitters, controlled by measurement outcomes. The array includes $M-1$ undisplaced thermal output idler modes and a single relevant output idler mode, subject to collective displacement.

A.2 Quantum Chernoff bound

The Quantum Chernoff Bound (QCB) is a powerful tool for determining an upper bound to the Helstrom limit $P_{\rm H}$ [155]–[158]. It is particularly useful for an ensemble of Gaussian states $\{\rho_h\}$, where it can be efficiently computed using symplectic decomposition. In our specific case of discriminating between $\Phi_{0,0}$ and $\Phi_{\kappa,0}$, this corresponds to the discrimination of $\{\rho_h\}_{h=0}^{\kappa}$, with mean $\bar{\mathbf{x}}_h = 0$ and CM $\mathbf{V}_{AI}^{\prime(h)}$ [see Eq. (2.18) with $\theta = 0$]. Indeed, the matrix $\mathbf{V}_{AI}^{\prime(h)}$ can be denoted as

$$\mathbf{V}_{AI}^{\prime(h)} = \begin{pmatrix} a_h\mathbf{I} & c_h\mathbf{Z} \\ c_h\mathbf{Z} & b\mathbf{I}, \end{pmatrix}, \tag{A.5}$$

with $a_h = 2N_A' + 1$, $b = 2N_I' + 1$, and $c_h = V_{12}'$. Its symplectic eigenspectrum is then given by

$$\nu_{\pm}^{(h)} = \frac{\sqrt{y_h} \pm (b - a_h)}{2}, \tag{A.6}$$

where $y_h = (a_h + b)^2 - 4c_h^2$, and with the symplectic matrix $\mathbf{S}_h$ described by

$$\mathbf{S}_h = \begin{pmatrix} \omega_+^{(h)}\mathbf{I} & \omega_-^{(h)}\mathbf{Z} \\ \omega_-^{(h)}\mathbf{Z} & \omega_+^{(h)}\mathbf{I}, \end{pmatrix}, \quad \omega_\pm^{(h)} = \sqrt{\frac{a_h + b \pm \sqrt{y_h}}{2\sqrt{y_h}}}. \tag{A.7}$$

In this regard, the QCB is simply expressed as

$$P_{\mathrm{QCB}} = \frac{1}{2}\left(\inf_{s\in[0,1]} \overline{Q}_s\right)^M, \tag{A.8}$$

where $\overline{Q}_s = 4\det(\mathbf{\Sigma}_s)^{-1/2}\prod_{j=1}^2 G_s\left(\nu_j^{(0)}\right) G_{1-s}\left(\nu_j^{(\kappa)}\right)$, $\mathbf{\Sigma}_s = \widetilde{\mathbf{V}}_0(s) + \widetilde{\mathbf{V}}_\kappa(1-s)$, and having defined

$$\begin{aligned} \widetilde{\mathbf{V}}_h(s) &= \mathbf{S}_h\left[\bigoplus_{j=1}^2 \Lambda_s\left(\nu_j^{(h)}\right)\mathbf{I}\right]\mathbf{S}_h^T, \\ G_s(x) &= \frac{2^s}{(x+1)^s - (x-1)^s}, \\ \Lambda_s(x) &= \frac{(x+1)^s + (x-1)^s}{(x+1)^s - (x-1)^s}. \end{aligned} \tag{A.9}$$

A.3 Phase-conjugate receiver

To ensure clarity and avoid confusion for the reader, we reintroduce the hat notation in this section, to distinguish between an operator $\hat{O}$ and its corresponding mean value $O = \langle\hat{O}\rangle$.

In a PCR the $\hat{a}'_A$ modes are phase-conjugated according to the following transformation

$$\hat{a}_C = \sqrt{G_{\mathrm{PCR}}}\hat{a}_{V_{\mathrm{PCR}}} + \sqrt{G_{\mathrm{PCR}} - 1}\hat{a}_A'^\dagger, \tag{A.10}$$

where G_{PCR} is the gain and $\hat{a}_{V_{\mathrm{PCR}}}$ is the annihilation operator of the noise entering the unused port of the PCR. The conjugated modes are then recombined on a balanced beamsplitter with the non-ideal idler mode $\hat{a}'_I$ as $\hat{a}_\pm = \left(\hat{a}_C \pm \hat{a}'_I\right)/\sqrt{2}$, that is

$$\hat{a}_\pm = \frac{1}{\sqrt{2}}\left(\sqrt{G_{\mathrm{PCR}}}\hat{a}_{V_{\mathrm{PCR}}} + \sqrt{G_{\mathrm{PCR}} - 1}\hat{a}_A'^\dagger \pm \hat{a}'_I\right). \tag{A.11}$$

In the following analysis, we will not consider terms whose mean value $\langle\cdot\rangle$ is null, such as those linear in $\hat{a}_{V_{\mathrm{PCR}}}$. Similarly, we will group together terms whose mean value $\langle\cdot\rangle$ is equal, that is, $\left\langle\hat{a}'_A\hat{a}'_I\right\rangle = \left\langle\hat{a}_I'^\dagger\hat{a}_A'^\dagger\right\rangle$. That said, the photon numbers at the output of the beamsplitter can be expressed as

$$\begin{aligned} \hat{N}_\pm &= \hat{a}_\pm^\dagger\hat{a}_\pm \\ &= \frac{1}{2}\left[\hat{N}_C \pm 2\sqrt{G_{\mathrm{PCR}} - 1}\hat{a}'_A\hat{a}'_I + \hat{N}'_I\right], \end{aligned} \tag{A.12}$$

where

$$\begin{aligned}\hat{N}_C &= \hat{a}_C^\dagger \hat{a}_C \\ &= G_{\mathrm{PCR}} \hat{N}_{V_{\mathrm{PCR}}} + (G_{\mathrm{PCR}} - 1)\left(\hat{N}'_A + 1\right), \\ \hat{N}_{V_{\mathrm{PCR}}} &= \hat{a}_{V_{\mathrm{PCR}}}^\dagger \hat{a}_{V_{\mathrm{PCR}}}.\end{aligned} \tag{A.13}$$

When $M \gg 1$, the photo-count difference $N = N_+ - N_-$, according to the central limit theorem, follows a Gaussian distribution with mean $M\mu$, where

$$\mu = \sqrt{G_{\mathrm{PCR}} - 1} V'_{12}, \tag{A.14}$$

and variance $M\sigma^2$, with

$$\begin{aligned}\sigma^2 &= N_+ (N_+ + 1) + N_- (N_- + 1) - \left(N_C - N'_I\right)^2 /2 \\ &= G_{\mathrm{PCR}} N_{V_{\mathrm{PCR}}} + (G_{\mathrm{PCR}} - 1)\left(N'_A + 1\right) + N'_I \\ &+ 2 (G_{\mathrm{PCR}} - 1)\left(N'_A + 1\right) N'_I + (G_{\mathrm{PCR}} - 1) V'^2_{12}/2.\end{aligned} \tag{A.15}$$

The values of the mean μ and the variance σ^2 are influenced by both the off-diagonal CM element V'_{12} and N'_A, which vary depending on whether the target is present (H_1) or absent (H_0). Using the Gaussian approximation, in the QI scenario, the error probability is simply given by

$$P_{\mathrm{E,PCR}} = \frac{1}{2} \operatorname{erfc}\left(\sqrt{R_{\mathrm{PCR}} M}\right), \quad R_{\mathrm{PCR}} = \frac{(\mu_1 - \mu_0)^2}{4\left(\sigma_1^2 + \sigma_0^2\right)}, \tag{A.16}$$

where the mean and variance for the two hypotheses are given by

$$\begin{aligned}\mu_0 &= 0, \\ \mu_1 &= 2\sqrt{\eta_S \eta_I G (G_{\mathrm{PCR}} - 1) \kappa N_S (N_S + 1)}, \\ \sigma_0^2 &= N'_I + (G_{\mathrm{PCR}} - 1)\left(2N'_I + 1\right)\left(N'_{A,\,\kappa=0} + 1\right) + G_{\mathrm{PCR}} N_{V_{\mathrm{PCR}}}, \\ \sigma_1^2 &= N'_I + (G_{\mathrm{PCR}} - 1)\left(2N'_I + 1\right)\left(N'_A + 1\right) + G_{\mathrm{PCR}} N_{V_{\mathrm{PCR}}} + \mu_1^2/2,\end{aligned} \tag{A.17}$$

resulting in the expression given for R_{PCR} in the main text.

References

[1] J. I. Cirac, P. Zoller, H. J. Kimble, and H. Mabuchi, "Quantum state transfer and entanglement distribution among distant nodes in a quantum network," *Phys. Rev. Lett.*, vol. 78, pp. 3221–3224, 1997. DOI: 10.1103/PhysRevLett.78.3221.

[2] T. Northup and R. Blatt, "Quantum information transfer using photons," *Nat. Photonics*, vol. 8, pp. 356–363, 2014. DOI: 10.1038/nphoton.2014.53.

[3] A. Reiserer and G. Rempe, "Cavity-based quantum networks with single atoms and optical photons," *Rev. Mod. Phys.*, vol. 87, pp. 1379–1418, 2015. DOI: 10.1103/RevModPhys.87.1379.

[4] D. Awschalom, K. K. Berggren, H. Bernien, *et al.*, "Development of quantum interconnects (quics) for next-generation information technologies," *PRX Quantum*, vol. 2, p. 017 002, 2021. DOI: 10.1103/PRXQuantum.2.017002.

[5] D. Moehring, P. Maunz, S. Olmschenk, *et al.*, "Entanglement of single-atom quantum bits at a distance," *Nature*, vol. 449, pp. 68–71, 2007. DOI: 10.1038/nature06118.

[6] S. Ritter, C. Nölleke, C. Hahn, *et al.*, "An elementary quantum network of single atoms in optical cavities," *Nature*, vol. 484, pp. 195–200, 2012. DOI: 10.1038/nature11023.

[7] B. Hensen, H. Bernien, A. E. Dréau, *et al.*, "Loophole-free bell inequality violation using electron spins separated by 1.3 kilometres," *Nature*, vol. 526, pp. 682–686, 2015. DOI: 10.1038/nature15759.

[8] R. Riedinger, A. Wallucks, I. Marinkovic, *et al.*, "Remote quantum entanglement between two micromechanical oscillators," *Nature*, vol. 556, 2018. DOI: 10.1038/s41586-018-0036-z.

[9] P. Kurpiers, P. Magnard, T. Walter, *et al.*, "Deterministic quantum state transfer and generation of remote entanglement using microwave photons," *Nature*, vol. 558, 2018. DOI: 10.1038/s41586-018-0195-y.

[10] K. Fedorov, M. Renger, S. Pogorzalek, *et al.*, "Experimental quantum teleportation of propagating microwaves," *Sci. Adv.*, vol. 7, 2021. DOI: 10.1126/sciadv.abk0891.

[11] M. Pompili, S. Hermans, S. Baier, *et al.*, "Realization of a multinode quantum network of remote solid-state qubits," *Science*, vol. 372, pp. 259–264, 2021. DOI: 10.1126/science.abg1919.

[12] V. Krutyanskiy, M. Galli, V. Krcmarsky, *et al.*, "Entanglement of trapped-ion qubits separated by 230 meters," *Phys. Rev. Lett.*, vol. 130, 2023. DOI: 10.1103/physrevlett.130.050803.

[13] R. Sahu, L. Qiu, W. Hease, *et al.*, "Entangling microwaves with light," *Science*, vol. 380, pp. 718–721, 2023. DOI: 10.1126/science.adg3812.

[14] J. F. Poyatos, J. I. Cirac, and P. Zoller, "Quantum reservoir engineering with laser cooled trapped ions," *Phys. Rev. Lett.*, vol. 77, pp. 4728–4731, 1996. DOI: 10.1103/PhysRevLett.77.4728.

[15] M. B. Plenio and S. F. Huelga, "Entangled light from white noise," *Phys. Rev. Lett.*, vol. 88, p. 197 901, 2002. DOI: 10.1103/PhysRevLett.88.197901.

[16] B. Kraus and J. I. Cirac, "Discrete Entanglement Distribution with Squeezed Light," *Phys. Rev. Lett.*, vol. 92, p. 013 602, 2004. DOI: 10.1103/PhysRevLett.92.013602.

[17] K. Stannigel, P. Rabl, and P. Zoller, "Driven-dissipative preparation of entangled states in cascaded quantum-optical networks," *New J. Phys.*, vol. 14, p. 063 014, 2012. DOI: 10.1088/1367-2630/14/6/063014.

[18] S. G. Schirmer and X. Wang, "Stabilizing open quantum systems by markovian reservoir engineering," *Phys. Rev. A*, vol. 81, p. 062 306, 2010. DOI: 10.1103/PhysRevA.81.062306.

[19] F. Motzoi, E. Halperin, X. Wang, K. B. Whaley, and S. Schirmer, "Backaction-driven, robust, steady-state long-distance qubit entanglement over lossy channels," *Phys. Rev. A*, vol. 94, p. 032 313, 2016. DOI: 10.1103/PhysRevA.94.032313.

[20] L. C. G. Govia, A. Lingenfelter, and A. A. Clerk, "Stabilizing two-qubit entanglement by mimicking a squeezed environment," *Phys. Rev. Res.*, vol. 4, p. 023 010, 2022. DOI: 10.1103/PhysRevResearch.4.023010.

[21] T. Brown, E. Doucet, D. Ristè, *et al.*, "Trade off-free entanglement stabilization in a superconducting qutrit-qubit system," *Nat. Commun.*, vol. 13, p. 3994, 2022. DOI: 10.1038/s41467-022-31638-0.

[22] E. Doucet, F. Reiter, L. Ranzani, and A. Kamal, "High fidelity dissipation engineering using parametric interactions," *Phys. Rev. Res.*, vol. 2, p. 023 370, 2020. DOI: 10.1103/PhysRevResearch.2.023370.

[23] S. Ma, X. Li, X. Liu, J. Xie, and F. Li, "Stabilizing bell states of two separated superconducting qubits via quantum reservoir engineering," *Phys. Rev. A*, vol. 99, p. 042 336, 2019. DOI: 10.1103/PhysRevA.99.042336.

[24] S. Ma, J. Zhang, X. Li, *et al.*, "Coupling-modulation–mediated generation of stable entanglement of superconducting qubits via dissipation," *EPL*, vol. 135, p. 63 001, 2021. DOI: 10.1209/0295-5075/ac2b5c.

[25] J. Agustí, Y. Minoguchi, J. M. Fink, and P. Rabl, "Long-distance distribution of qubit-qubit entanglement using gaussian-correlated photonic beams," *Phys. Rev. A*, vol. 105, p. 062 454, 2022. DOI: 10.1103/PhysRevA.105.062454.

[26] K. P. Horn, F. Reiter, Y. Lin, D. Leibfried, and C. P. Koch, "Quantum optimal control of the dissipative production of a maximally entangled state," *New J. Phys.*, vol. 20, p. 123 010, 2018. DOI: 10.1088/1367-2630/aaf360.

[27] S. Diehl, A. Micheli, A. Kantian, B. Kraus, H. P. Büchler, and P. Zoller, "Quantum States and Phases in Driven Open Quantum Systems with Cold Atoms," *Nat. Phys.*, vol. 4, pp. 878–883, 2008. DOI: 10.1038/nphys1073.

[28] A. Pocklington, Y. X. Wang, Y. Yanay, and A. A. Clerk, "Stabilizing volume-law entangled states of fermions and qubits using local dissipation," *Phys. Rev. B*, vol. 105, p. L140301, 2022. DOI: 10.1103/PhysRevB.105.L140301.

[29] S. Zippilli, J. Li, and D. Vitali, "Steady-state nested entanglement structures in harmonic chains with single-site squeezing manipulation," *Phys. Rev. A*, vol. 92, p. 032 319, 2015. DOI: 10.1103/PhysRevA.92.032319.

[30] J. Angeletti, S. Zippilli, and D. Vitali, "Dissipative stabilization of entangled qubit pairs in quantum arrays with a single localized dissipative channel," *Quantum Sci. Technol.*, vol. 8, p. 035 020, 2023. DOI: 10.1088/2058-9565/acd4e3.

[31] S. Zippilli, M. Paternostro, G. Adesso, and F. Illuminati, "Entanglement Replication in Driven Dissipative Many-Body systems," *Phys. Rev. Lett.*, vol. 110, p. 040 503, 2013. DOI: 10.1103/PhysRevLett.110.040503.

[32] Y. Yanay and A. A. Clerk, "Reservoir engineering of bosonic lattices using chiral symmetry and localized dissipation," *Phys. Rev. A*, vol. 98, p. 043 615, 2018. DOI: 10.1103/PhysRevA.98.043615.

[33] S. Zippilli and D. Vitali, "Dissipative Engineering of Gaussian Entangled States in Harmonic Lattices with a Single-Site Squeezed Reservoir," *Phys. Rev. Lett.*, vol. 126, p. 020 402, 2021. DOI: 10.1103/PhysRevLett.126.020402.

[34] S. Ma, M. J. Woolley, I. R. Petersen, and N. Yamamoto, "Pure Gaussian states from quantum harmonic oscillator chains with a single local dissipative process," *J. Phys. A: Math. Theor.*, vol. 50, p. 135 301, 2017. DOI: 10.1088/1751-8121/aa5fbe.

[35] M. Žnidarič, "Exact solution for a diffusive nonequilibrium steady state of an open quantum chain," *J. Stat. Mech.*, vol. 2010, p. L05002, 2010. DOI: 10.1088/1742-5468/2010/05/L05002.

[36] T. Prosen, "Third quantization: A general method to solve master equations for quadratic open fermi systems," *New J. Phys.*, vol. 10, p. 043 026, 2008. DOI: 10.1088/1367-2630/10/4/043026.

[37] H. Sigurdsson, A. J. Ramsay, H. Ohadi, *et al.*, "Driven-dissipative spin chain model based on exciton-polariton condensates," *Phys. Rev. B*, vol. 96, p. 155 403, 2017. DOI: 10.1103/PhysRevB.96.155403.

[38] V. Y. Popkov, D. Karevski, and G. Schütz, "Exact Results for the Isotropic Spin-1/2 Heisenberg Chain With Dissipative Boundary Driving," *Theor. Math. Phys.*, vol. 198, pp. 296–315, 2019. DOI: 10.1134/S0040577919020107.

[39] K. Yamanaka and T. Sasamoto, *Exact solution for the lindbladian dynamics for the open xx spin chain with boundary dissipation*, 2023. DOI: 10.48550/arXiv.2104.11479.

[40] M. Žnidarič, T. Prosen, and P. Prelovšek, "Many-body localization in the heisenberg *XXZ* magnet in a random field," *Phys. Rev. B*, vol. 77, p. 064 426, 2008. DOI: 10.1103/PhysRevB.77.064426.

[41] M. Žnidarič, "Relaxation times of dissipative many-body quantum systems," *Phys. Rev. E*, vol. 92, p. 042 143, 2015. DOI: 10.1103/PhysRevE.92.042143.

[42] M. V. Medvedyeva and S. Kehrein, "Power-law approach to steady state in open lattices of noninteracting electrons," *Phys. Rev. B*, vol. 90, p. 205 410, 2014. DOI: 10.1103/PhysRevB.90.205410.

[43] T. Prosen and I. Pižorn, "Quantum phase transition in a far-from-equilibrium steady state of an *XY* spin chain," *Phys. Rev. Lett.*, vol. 101, p. 105 701, 2008. DOI: 10.1103/PhysRevLett.101.105701.

[44] T. Prosen and M. Žnidarič, "Matrix product simulations of non-equilibrium steady states of quantum spin chains," *J. Stat. Mech.*, vol. 2009, P02035, 2009. DOI: 10.1088/1742-5468/2009/02/P02035.

[45] T. Prosen, "Open *XXZ* spin chain: Nonequilibrium steady state and a strict bound on ballistic transport," *Phys. Rev. Lett.*, vol. 106, p. 217 206, 2011. DOI: 10.1103/PhysRevLett.106.217206.

[46] C. D. Parmee and N. R. Cooper, "Steady states of a driven dissipative dipolar xxz chain," *J. Phys. B: At. Mol. Opt. Phys.*, vol. 53, p. 135 302, 2020. DOI: 10.1088/1361-6455/ab8949.

[47] G. Vitagliano, A. Riera, and J. I. Latorre, "Volume-law scaling for the entanglement entropy in spin-1/2 chains," *New J. Phys.*, vol. 12, p. 113 049, 2010. DOI: 10.1088/1367-2630/12/11/113049.

[48] M. B. Plenio, S. F. Huelga, A. Beige, and P. L. Knight, "Cavity-loss-induced generation of entangled atoms," *Phys. Rev. A*, vol. 59, p. 2468, 1999. DOI: 10.1103/PhysRevA.59.2468.

[49] B. Kraus, H. P. Büchler, S. Diehl, A. Kantian, A. Micheli, and P. Zoller, "Preparation of entangled states by quantum Markov processes," *Phys. Rev. A*, vol. 78, p. 042 307, 2008. DOI: 10.1103/PhysRevA.78.042307.

[50] F. Verstraete, M. M. Wolf, and J. I. Cirac., "Quantum computation and quantum-state engineering driven by dissipation," *Nat. Phys.*, vol. 5, pp. 633–636, 2009. DOI: 10.1038/nphys1342.

[51] H. Weimer, M. Müller, I. Lesanovsky, P. Zoller, and H. P. Büchler, "A Rydberg quantum simulator," *Nat. Phys.*, vol. 6, pp. 382–388, 2010. DOI: 10.1038/nphys1614.

[52] J. T. Barreiro, M. Müller, P. Schindler, *et al.*, "An open-system quantum simulator with trapped ions," *Nature*, vol. 470, pp. 486–491, 2011. DOI: 10.1038/nature09801.

[53] J. Cho, S. Bose, and M. S. Kim, "Optical Pumping into Many-Body Entanglement," *Phys. Rev. Lett.*, vol. 106, p. 020 504, 2011. DOI: 10.1103/PhysRevLett.106.020504.

[54] K. Koga and N. Yamamoto, "Dissipation-induced pure Gaussian state," *Phys. Rev. A*, vol. 85, p. 022 103, 2012. DOI: 10.1103/PhysRevA.85.022103.

[55] G. Morigi, J. Eschner, C. Cormick, Y. Lin, D. Leibfried, and D. J. Wineland, "Dissipative Quantum Control of a Spin Chain," *Phys. Rev. Lett.*, vol. 115, p. 200 502, 2015. DOI: 10.1103/PhysRevLett.115.200502.

[56] F. Reiter, D. Reeb, and A. S. Sørensen, "Scalable Dissipative Preparation of Many-Body Entanglement," *Phys. Rev. Lett.*, vol. 117, p. 040 501, 2016. DOI: 10.1103/PhysRevLett.117.040501.

[57] S. Zippilli, M. Paternostro, G. Adesso, and F. Illuminati, "Erraturm: Entanglement Replication in Driven Dissipative Many-Body Systems," *Phys. Rev. Lett.*, vol. 111, p. 169 901, 2013. DOI: 10.1103/PhysRevLett.111.169901.

[58] S. Zippilli and F. Illuminati, "Non-Markovian dynamics and steady-state entanglement of cavity arrays in finite-bandwidth squeezed reservoirs," *Phys. Rev. A*, vol. 89, p. 033 803, 2014. DOI: 10.1103/PhysRevA.89.033803.

[59] S. Ma and M. J. Woolley, "Entangled pure steady states in harmonic chains with a two-mode squeezed reservoir," *J. Phys. A: Math. Theor.*, vol. 52, p. 325 301, 2019. DOI: 10.1088/1751-8121/ab2ce7.

[60] P. Wendenbaum, T. Platini, and D. Karevski, "Entanglement replication via quantum repeated interactions," *Phys. Rev. A*, vol. 91, p. 040 303, 2015. DOI: 10.1103/PhysRevA.91.040303.

[61] M. Asjad, S. Zippilli, and D. Vitali, "Mechanical Einstein-Podolsky-Rosen entanglement with a finite-bandwidth squeezed reservoir," *Phys. Rev. A*, vol. 93, p. 062 307, 2016. DOI: 10.1103/PhysRevA.93.062307.

[62] Y. Yanay and A. A. Clerk, "Reservoir engineering with localized dissipation: Dynamics and prethermalization," *Phys. Rev. Research*, vol. 2, p. 023 177, 2020. DOI: 10.1103/PhysRevResearch.2.023177.

[63] Y. Yanay, "Algorithm for tailoring a quadratic lattice with a local squeezed reservoir to stabilize generic chiral states with nonlocal entanglement," *Phys. Rev. A*, vol. 102, p. 032 417, 2020. DOI: 10.1103/PhysRevA.102.032417.

[64] J. B. Clark, F. Lecocq, R. W. Simmonds, J. Aumentado, and J. D. Teufel, "Sideband cooling beyond the quantum backaction limit with squeezed light," *Nature*, vol. 541, pp. 191–195, 2017. DOI: 10.1038/nature20604.

[65] F. Acernese, M. Agathos, L. Aiello, *et al.*, "Increasing the astrophysical reach of the advanced virgo detector via the application of squeezed vacuum states of light," *Phys. Rev. Lett.*, vol. 123, p. 231 108, 2019. DOI: 10.1103/PhysRevLett.123.231108.

[66] M. Tse, H. Yu, N. Kijbunchoo, *et al.*, "Quantum-enhanced advanced ligo detectors in the era of gravitational-wave astronomy," *Phys. Rev. Lett.*, vol. 123, p. 231 107, 2019. DOI: 10.1103/PhysRevLett.123.231107.

[67] G. Ramírez, J. Rodríguez-Laguna, and G. Sierra, "From conformal to volume law for the entanglement entropy in exponentially deformed critical spin 1/2 chains," *J. Stat. Mech.*, vol. 2014, p. 10 004, 2014. DOI: 10.1088/1742-5468/2014/10/P10004.

[68] C. M. Langlett, Z. C. Yang, J. W. A. V. Gorshkov, T. Iadecola, and S. Xu, "Rainbow scars: From area to volume law," *Phys. Rev. B*, vol. 105, p. L060301, 2022. DOI: 10.1103/PhysRevB.105.L060301.

[69] S. Zippilli, S. M. Giampaolo, and F. Illuminati, "Surface entanglement in quantum spin networks," *Phys. Rev. A*, vol. 87, p. 042 304, 2013. DOI: 10.1103/PhysRevA.87.042304.

[70] C. D. Franco, M. Paternostro, and M. S. Kim, "Nested entangled states for distributed quantum channels," *Phys. Rev. A*, vol. 77, p. 020 303, 2008. DOI: 10.1103/PhysRevA.77.020303.

[71] L. B. B. Alkurtass and S. Bose, "Optimal quench for distance-independent entanglement and maximal block entropy," *Phys. Rev. A*, vol. 90, p. 042 304, 2014. DOI: 10.1103/PhysRevA.90.042304.

[72] I. Pitsios, L. Banchi, A. S. Rab, *et al.*, "Photonic simulation of entanglement growth and engineering after a spin chain quench," *Nat. Commun.*, vol. 8, p. 1569, 2017. DOI: 10.1038/s41467-017-01589-y.

[73] W. Cottrell, B. Freivogel, D. M. Hofman, and S. F. Lokhande, "How to build the thermofield double state," *J. High Energ. Phys.*, vol. 2019, p. 58, 2019. DOI: 10.1007/JHEP02(2019)058.

[74] A. R. Brown, H. Gharibyan, S. Leichenauer, *et al.*, "Quantum Gravity in the Lab: Teleportation by Size and Traversable Wormholes," *PRX Quantum*, vol. 4, p. 010 320, 2023. DOI: 10.1103/PRXQuantum.4.010320.

[75] S. Dutta and N. R. Cooper, "Long-Range Coherence and Multiple Steady States in a Lossy Qubit Array," *Phys. Rev. Lett.*, vol. 125, p. 240 404, 2020. DOI: 10.1103/PhysRevLett.125.240404.

[76] S. Dutta and N. R. Cooper, "Out-of-equilibrium steady states of a locally driven lossy qubit array," *Phys. Rev. Research*, vol. 3, p. L012016, 2021. DOI: 10.1103/PhysRevResearch.3.L012016.

[77] R. Horodecki, P. Horodecki, M. Horodecki, and K. Horodecki, "Quantum entanglement," *Rev. Mod. Phys.*, vol. 81, pp. 865–942, 2009. DOI: 10.1103/RevModPhys.81.865.

[78] M. Asjad, S. Zippilli, and D. Vitali, "Suppression of stokes scattering and improved optomechanical cooling with squeezed light," *Phys. Rev. A*, vol. 94, p. 051 801, 2016. DOI: 10.1103/PhysRevA.94.051801.

[79] J. O. González, L. A. Correa, G. Nocerino, J. P. Palao, D. Alonso, and G. Adesso, "Testing the validity of the 'local' and 'global' gkls master equations on an exactly solvable model," *Open Syst. Inf. Dyn.*, vol. 24, p. 1 740 010, 2017. DOI: 10.1142/S1230161217400108.

[80] P. P. Hofer, M. Perarnau-Llobet, L. David, *et al.*, "Markovian master equations for quantum thermal machines: Local versus global approach," *New J. Phys.*, vol. 19, p. 123 037, 2017. DOI: 10.1088/1367-2630/aa964f.

[81] M. Cattaneo, G. L. Giorgi, S. Maniscalco, and R. Zambrini, "Local versus global master equation with common and separate baths: Superiority of the global approach in partial secular approximation," *New J. Phys.*, vol. 21, p. 113 045, 2019. DOI: 10.1088/1367-2630/ab54ac.

[82] S. Scali, J. Anders, and L. A. Correa, "Local master equations bypass the secular approximation," *Quantum*, vol. 5, p. 451, 2021. DOI: 10.22331/q-2021-05-01-451.

[83] F. Benatti, R. Floreanini, and M. Piani, "Environment Induced Entanglement in Markovian Dissipative Dynamics," *Phys. Rev. Lett.*, vol. 91, p. 070 402, 2003. DOI: 10.1103/PhysRevLett.91.070402.

[84] M. Paternostro, W. Son, and M. S. Kim, "Complete Conditions for Entanglement Transfer," *Phys. Rev. Lett.*, vol. 92, p. 197 901, 2004. DOI: 10.1103/PhysRevLett.92.197901.

[85] G. Adesso, S. Campbell, F. Illuminati, and M. Paternostro, "Controllable Gaussian-Qubit Interface for Extremal Quantum State Engineering," *Phys. Rev. Lett.*, vol. 104, p. 240 501, 2010. DOI: 10.1103/PhysRevLett.104.240501.

[86] J. Zhang, G. Pagano, P. W. Hess, *et al.*, "Observation of a Many-Body Dynamical Phase Transition with a 53-Qubit Quantum Simulator," *Nature*, vol. 551, pp. 601–604, 2017. DOI: 10.1038/nature24654.

[87] T. Brydges, A. Elben, P. Jurcevic, *et al.*, "Probing Rényi entanglement entropy via randomized measurements," *Science*, vol. 364, pp. 260–263, 2019. DOI: 10.1126/science.aau4963.

[88] C. Kokail, C. Maier, R. van Bijnen, *et al.*, "Self-verifying variational quantum simulation of lattice models," *Nature*, vol. 569, pp. 355–360, 2019. DOI: 10.1038/s41586-019-1177-4.

[89] C. D. Bruzewicz, J. Chiaverini, R. McConnell, and J. M. Sage, "Trapped-Ion Quantum Computing: Progress and Challenges," *Appl. Phys. Rev.*, vol. 6, p. 021 314, 2019. DOI: 10.1063/1.5088164.

[90] M. Tomza, K. Jachymski, R. Gerritsma, *et al.*, "Cold hybrid ion-atom systems," *Rev. Mod. Phys.*, vol. 91, p. 035 001, 2019. DOI: 10.1103/RevModPhys.91.035001.

[91] S. Hacohen-Gourgy, V. V. Ramasesh, C. D. Grandi, I. Siddiqi, and S. M. Girvin, "Cooling and Autonomous Feedback in a Bose-Hubbard Chain with Attractive Interactions," *Phys. Rev. Lett.*, vol. 115, p. 240 501, 2015. DOI: 10.1103/PhysRevLett.115.240501.

[92] M. Fitzpatrick, N. M. Sundaresan, A. C. Y. Li, J. Koch, and A. A. Houck, "Observation of a Dissipative Phase Transition in a One-Dimensional Circuit QED Lattice," *Phys. Rev. X*, vol. 7, p. 011 016, 2017. DOI: 10.1103/PhysRevX.7.011016.

[93] P. Roushan, C. Neill, J. Tangpanitanon, *et al.*, "Spectroscopic signatures of localization with interacting photons in superconducting qubits," *Science*, vol. 358, pp. 1175–1179, 2017. DOI: 10.1126/science.aao1401.

[94] A. J. Kollár, M. Fitzpatrick, and A. A. Houck, "Hyperbolic lattices in circuit quantum electrodynamics," *Nature*, vol. 571, pp. 45–50, 2019. DOI: 10.1038/s41586-019-1348-3.

[95] R. Ma, B. Saxberg, C. Owens, *et al.*, "A dissipatively stabilized Mott insulator of photons," *Nature*, vol. 566, pp. 51–57, 2019. DOI: 10.1038/s41586-019-0897-9.

[96] A. Smith, B. Jobst, A. G. Green, and F. Pollmann, "Crossing a topological phase transition with a quantum computer," *Phys. Rev. Research*, vol. 4, p. L022020, 2022. DOI: 10.1103/PhysRevResearch.4.L022020.

[97] E. Kim, X. Zhang, V. S. Ferreira, *et al.*, "Quantum Electrodynamics in a Topological Waveguide," *Phys. Rev. X*, vol. 11, p. 011 015, 2021. DOI: 10.1103/PhysRevX.11.011015.

[98] K. L. Hur, L. Henriet, A. Petrescu, K. Plekhanov, G. Roux, and M. Schiró, "Many-body quantum electrodynamics networks: Non-equilibrium condensed matter physics with light," *C. R. Physique*, vol. 17, pp. 808–835, 2016. DOI: 10.1016/j.crhy.2016.05.003.

[99] X. Gu, A. F. Kockum, A. Miranowicz, Y. X. Liu, and F. Nori, "Microwave photonics with superconducting quantum circuits," *Phys. Rep.*, vol. 718–719, pp. 1–102, 2017. DOI: 10.1016/j.physrep.2017.10.002.

[100] G. Wendin, "Quantum information processing with superconducting circuits: A review," *Rep. Prog. Phys.*, vol. 80, p. 106 001, 2017. DOI: 10.1088/1361-6633/aa7e1a.

[101] T. Ozawa, H. M. Price, A. Amo, *et al.*, "Topological photonics," *Rev. Mod. Phys.*, vol. 91, p. 015 006, 2019. DOI: 10.1103/RevModPhys.91.015006.

[102] I. Carusotto, A. A. Houck, A. J. Kollár, P. Roushan, D. I. Schuster, and J. Simon, "Photonic materials in circuit quantum electrodynamics," *Nat. Phys.*, vol. 16, pp. 268–279, 2020. DOI: 10.1038/s41567-020-0815-y.

[103] S. A. Wilkinson and M. J. Hartmann, "Superconducting quantum many-body circuits for quantum simulation and computing," *Appl. Phys. Lett.*, vol. 116, p. 230 501, 2020. DOI: 10.1063/5.0008202.

[104] M. Hein, W. Dür, J. Eisert, R. Raussendorf, M.Van den Nest, and H. J. Briegel, "Entanglement in graph states and its applications," *Proc. Int. Sch. Phys. Enrico Fermi*, vol. 162, pp. 115–218, 2006. DOI: 10.3254/978-1-61499-018-5-115.

[105] M. F. Sacchi, "Entanglement can enhance the distinguishability of entanglement-breaking channels," *Phys. Rev. A*, vol. 72, p. 014 305, 2005. DOI: 10.1103/PhysRevA.72.014305.

[106] S. Lloyd, "Enhanced sensitivity of photodetection via quantum illumination," *Science*, vol. 321, pp. 1463–1465, 2008. DOI: 10.1126/science.1160627.

[107] S.-H. Tan, B. I. Erkmen, V. Giovannetti, *et al.*, "Quantum illumination with gaussian states," *Phys. Rev. Lett.*, vol. 101, p. 253 601, 2008. DOI: 10.1103/PhysRevLett.101.253601.

[108] S. Barzanjeh, S. Guha, C. Weedbrook, D. Vitali, J. H. Shapiro, and S. Pirandola, "Microwave quantum illumination," *Phys. Rev. Lett.*, vol. 114, p. 080 503, 2015. DOI: 10.1103/PhysRevLett.114.080503.

[109] C. W. Helstrom, *Quantum Detection and Estimation Theory* (Mathematics in Science and Engineering: a series of monographs and textbooks). Academic Press, 1976. [Online]. Available: https://books.google.com/books?id=fv9SAAAAMAAJ.

[110] H. Chernoff, "A Measure of Asymptotic Efficiency for Tests of a Hypothesis Based on the sum of Observations," *Ann. Math. Statist.*, vol. 23, pp. 493–507, 1952. DOI: 10.1214/aoms/1177729330.

[111] E. D. Lopaeva, I. Ruo-Berchera, I. P. Degiovanni, S. Olivares, G. Brida, and M. Genovese, "Experimental realization of quantum illumination," *Phys. Rev. Lett.*, vol. 110, p. 153 603, 2013. DOI: 10.1103/PhysRevLett.110.153603.

[112] Z. Zhang, M. Tengner, T. Zhong, F. N. C. Wong, and J. H. Shapiro, "Entanglement's benefit survives an entanglement-breaking channel," *Phys. Rev. Lett.*, vol. 111, p. 010 501, 2013. DOI: 10.1103/PhysRevLett.111.010501.

[113] Z. Zhang, S. Mouradian, F. N. C. Wong, and J. H. Shapiro, "Entanglement-enhanced sensing in a lossy and noisy environment," *Phys. Rev. Lett.*, vol. 114, p. 110 506, 2015. DOI: 10.1103/PhysRevLett.114.110506.

[114] D. G. England, B. Balaji, and B. J. Sussman, "Quantum-enhanced standoff detection using correlated photon pairs," *Phys. Rev. A*, vol. 99, p. 023 828, 2019. DOI: 10.1103/PhysRevA.99.023828.

[115] C. W. S. Chang, A. M. Vadiraj, J. Bourassa, B. Balaji, and C. M. Wilson, "Quantum-enhanced noise radar," *Appl. Phys. Lett.*, vol. 114, p. 112 601, 2019. DOI: 10.1063/1.5085002.

[116] D. Luong, C. W. S. Chang, A. M. Vadiraj, A. Damini, C. M. Wilson, and B. Balaji, "Receiver operating characteristics for a prototype quantum two-mode squeezing radar," *IEEE Trans. Aerosp. Electron. Syst.*, vol. 56, pp. 2041–2060, 2020. DOI: 10.1109/TAES.2019.2951213.

[117] S. Barzanjeh, S. Pirandola, D. Vitali, and J. M. Fink, "Microwave quantum illumination using a digital receiver," *Sci. Adv.*, vol. 6, 2020. DOI: 10.1126/sciadv.abb0451.

[118] R. Assouly, R. Dassonneville, T. Peronnin, A. Bienfait, and B. Huard, "Quantum advantage in microwave quantum radar," *Nat. Phys.*, vol. 19, pp. 1418–1422, 2023. DOI: 10.1038/s41567-023-02113-4.

[119] Q. Zhuang, Z. Zhang, and J. H. Shapiro, "Quantum illumination for enhanced detection of rayleigh-fading targets," *Phys. Rev. A*, vol. 96, p. 020 302, 2017. DOI: 10.1103/PhysRevA.96.020302.

[120] S. Pirandola, B. R. Bardhan, T. Gehring, C. Weedbrook, and S. Lloyd, "Advances in photonic quantum sensing," *Nat. Photonics*, vol. 12, pp. 724–733, 2018. DOI: 10.1038/s41566-018-0301-6.

[121] J. H. Shapiro, "The quantum illumination story," *IEEE Trans. Aerosp. Electron. Syst.*, vol. 35, pp. 8–20, 2020. DOI: 10.1109/MAES.2019.2957870.

[122] Q. Zhuang, "Quantum ranging with gaussian entanglement," *Phys. Rev. Lett.*, vol. 126, p. 240 501, 2021. DOI: 10.1103/PhysRevLett.126.240501.

[123] Q. Zhuang and J. H. Shapiro, "Ultimate accuracy limit of quantum pulse-compression ranging," *Phys. Rev. Lett.*, vol. 128, p. 010 501, 2022. DOI: 10.1103/PhysRevLett.128.010501.

[124] A. V. Dixit, S. Chakram, K. He, *et al.*, "Searching for dark matter with a superconducting qubit," *Phys. Rev. Lett.*, vol. 126, p. 141 302, 2021. DOI: 10.1103/PhysRevLett.126.141302.

[125] N. Lauk, N. Sinclair, S. Barzanjeh, *et al.*, "Perspectives on quantum transduction," *Quantum Sci. Technol.*, vol. 5, p. 020 501, 2020. DOI: 10.1088/2058-9565/ab788a.

[126] L. Fan, C.-L. Zou, R. Cheng, *et al.*, "Superconducting cavity electro-optics: A platform for coherent photon conversion between superconducting and photonic circuits," *Sci. Adv.*, vol. 4, eaar4994, 2018. DOI: 10.1126/sciadv.aar4994.

[127] X. Han, W. Fu, C.-L. Zou, L. Jiang, and H. X. Tang, "Microwave-optical quantum frequency conversion," *Optica*, vol. 8, no. 8, pp. 1050–1064, 2021. DOI: 10.1364/OPTICA.425414.

[128] B. M. Brubaker, J. M. Kindem, M. D. Urmey, *et al.*, "Optomechanical ground-state cooling in a continuous and efficient electro-optic transducer," *Phys. Rev. X*, vol. 12, p. 021 062, 2022. DOI: 10.1103/PhysRevX.12.021062.

[129] S. Guha and B. I. Erkmen, "Gaussian-state quantum-illumination receivers for target detection," *Phys. Rev. A*, vol. 80, p. 052 310, 2009. DOI: 10.1103/PhysRevA.80.052310.

[130] Q. Zhuang, Z. Zhang, and J. H. Shapiro, "Optimum mixed-state discrimination for noisy entanglement-enhanced sensing," *Phys. Rev. Lett.*, vol. 118, p. 040 801, 2017. DOI: 10.1103/PhysRevLett.118.040801.

[131] H. Shi, B. Zhang, and Q. Zhuang, "Fulfilling entanglement's benefit via converting correlation to coherence," *ArXiv:2207.06609*, 2022. DOI: 10.48550/arXiv.2207.06609.

[132] R. Nair and M. Gu, "Fundamental limits of quantum illumination," *Optica*, vol. 7, no. 7, pp. 771–774, 2020. DOI: 10.1364/OPTICA.391335.

[133] X.-S. Ma, S. Zotter, N. Tetik, A. Qarry, T. Jennewein, and A. Zeilinger, "A high-speed tunable beam splitter for feed-forward photonic quantum information processing," *Opt. Express*, vol. 19, pp. 22 723–22 730, 2011. DOI: 10.1364/OE.19.022723.

[134] G. Kraftmakher, V. Butylkin, Y. Kazantsev, and V. Mal'tsev, "New functionality in microwave interferometry by application of metastructure as a tunable beam-splitter," *J. Phys.: Conf. Ser.*, vol. 1461, p. 012 074, 2020. DOI: 10.1088/1742-6596/1461/1/012074.

[135] J. Angeletti, H. Shi, T. Lakshmanan, D. Vitali, and Q. Zhuang, "Microwave quantum illumination with correlation-to-displacement conversion," *Phys. Rev. Appl.*, vol. 20, p. 024 030, 2023. DOI: 10.1103/PhysRevApplied.20.024030.

[136] H. Shi, Z. Zhang, and Q. Zhuang, "Practical route to entanglement-assisted communication over noisy bosonic channels," *Phys. Rev. Appl.*, vol. 13, p. 034 029, 2020. DOI: 10.1103/PhysRevApplied.13.034029.

[137] G. D. Palma and J. Borregaard, "Minimum error probability of quantum illumination," *Phys. Rev. A*, vol. 98, p. 012 101, 2018. DOI: 10.1103/PhysRevA.98.012101.

[138] E. Flurin, N. Roch, F. Mallet, M. Devoret, and B. Huard, "Generating entangled microwave radiation over two transmission lines.," *Phys. Rev. Lett.*, vol. 109, p. 183 901, 2012. DOI: 10.1103/PhysRevLett.109.183901.

[139] B. Abdo, A. Kamal, and M. Devoret, "Nondegenerate three-wave mixing with the josephson ring modulator," *Phys. Rev. B*, vol. 87, p. 014 508, 2013. DOI: 10.1103/PhysRevB.87.014508.

[140] X. Chen and Q. Zhuang, "Entanglement-assisted detection of fading targets via correlation-to-displacement conversion," *Phys. Rev. A*, vol. 107, p. 062 405, 2023. DOI: 10.1103/PhysRevA.107.062405.

[141] C. W. Helstrom, "Minimum mean-squared error of estimates in quantum statistics," *Phys. Lett. A*, vol. 25, pp. 101–102, 1967. DOI: 10.1016/0375-9601(67)90366-0.

[142] C. W. Helstrom, "Quantum detection and estimation theory," *J. Stat. Phys.*, vol. 1, pp. 231–252, 1969. DOI: 10.1007/BF01007479.

[143] *Rising above the noise: Quantum-limited amplifiers empower the readout of ibm quantum systems, baleegh abdo*, https://www.ibm.com/blogs/research/2020/01/quantum-limited-amplifiers/, Accessed: 2022-01-15.

[144] K. M. R. Audenaert, J. Calsamiglia, R. Muñoz-Tapia, *et al.*, "Discriminating states: The quantum chernoff bound," *Phys. Rev. Lett.*, vol. 98, p. 160 501, 2007. DOI: 10.1103/PhysRevLett.98.160501.

[145] R. J. Glauber, "Coherent and incoherent states of the radiation field," *Phys. Rev.*, vol. 131, p. 2766, 1963. DOI: 10.1103/PhysRev.131.2766.

[146] M. Takeoka and M. Sasaki, "Discrimination of the binary coherent signal: Gaussian-operation limit and simple non-gaussian near-optimal receivers," *Phys. Rev. A*, vol. 78, p. 022 320, 2008. DOI: 10.1103/PhysRevA.78.022320.

[147] G. Lachs, "Theoretical aspects of mixtures of thermal and coherent radiation," *Phys. Rev.*, vol. 138, p. 1012, 1965. DOI: 10.1103/PhysRev.138.B1012.

[148] P. Marian and T. A. Marian, "Squeezed states with thermal noise. i. photon-number statistics," *Phys. Rev. A*, vol. 47, pp. 4474–4486, 1993. DOI: 10.1103/PhysRevA.47.4474.

[149] H. L. Van Trees, *Detection, estimation, and modulation theory, part III: Radar–sonar signal process. and gaussian signals in noise*, 2001. DOI: 10.1002/0471221082.

[150] G. Sorelli, N. Treps, F. Grosshans, and F. Boust, "Detecting a target with quantum entanglement," *IEEE Aerosp. Electron. Syst. Mag.*, vol. 37, pp. 68–90, 2022. DOI: 10.1109/MAES.2021.3116323.

[151] J. H. Shapiro, "Extended version of van trees's receiver operating characteristic approximation," *IEEE Trans. Aerosp. Electron. Syst.*, vol. 35, pp. 709–716, 1999. DOI: 10.1109/7.766950.

[152] L. Fan and M. S. Zubairy, "Quantum illumination using non-gaussian states generated by photon subtraction and photon addition," *Phys. Rev. A*, vol. 98, p. 012 319, 2018. DOI: 10.1103/PhysRevA.98.012319.

[153] R. Gupta, S. Roy, T. Das, and A. S. De, "Quantum illumination with noisy probes: Conditional advantages of non-gaussianity," *ArXiv:2107.02774*, 2021. DOI: 10.48550/arXiv.2107.02774.

[154] M. Bradshaw, L. O. Conlon, S. Tserkis, M. Gu, P. K. Lam, and S. M. Assad, "Optimal probes for continuous-variable quantum illumination," *Phys. Rev. A*, vol. 103, p. 062 413, 2021. DOI: 10.1103/PhysRevA.103.062413.

[155] L.-M. Duan, G. Giedke, J. I. Cirac, and P. Zoller, "Inseparability criterion for continuous variable systems," *Phys. Rev. Lett.*, vol. 84, pp. 2722–2725, 2000. DOI: 10.1103/PhysRevLett.84.2722.

[156] R. Simon, "Peres-horodecki separability criterion for continuous variable systems," *Phys. Rev. Lett.*, vol. 84, pp. 2726–2729, 12 2000. DOI: 10.1103/PhysRevLett.84.2726.

[157] S. Pirandola and S. Lloyd, "Computable bounds for the discrimination of gaussian states," *Phys. Rev. A*, vol. 78, p. 012 331, 2008. DOI: 10.1103/physreva.78.012331.

[158] C. Weedbrook, S. Pirandola, R. García-Patrón, *et al.*, "Gaussian quantum information," *Rev. Mod. Phys.*, vol. 84, p. 621, 2012. DOI: doi/10.1103/RevModPhys.84.621.